1 **Title**

2 **Insights into animal septins using recombinant human septin octamers**

3 **with distinct SEPT9 isoforms**

4

5 Francois Iv[1], Carla Silva Martins[1], Gerard Castro-Linares[2], Cyntia Taveneau[3,4], Pascale Barbier[5],

6 Pascal Verdier-Pinard[6], Luc Camoin[7], Stéphane Audebert[7], Feng-Ching Tsai[8,#], Laurie Ramond[1],

7 Alex Llewellyn[1], Mayssa Belhabib[1], Koyomi Nakazawa[3], Aurélie Di Cicco[3], Renaud Vincentelli[9],

8 Jerome Wenger[1], Stéphanie Cabantous[10], Gijsje H. Koenderink[2,8,*], Aurélie Bertin[3,*], Manos

9 Mavrakis[1,*]

10

11 [1] Institut Fresnel, CNRS UMR7249, Aix Marseille Univ, Centrale Marseille, 13013 Marseille, France

12 [2] Department of Bionanoscience, Kavli Institute of Nanoscience Delft, Delft University of Technology, 2629

13 HZ Delft, The Netherlands

14 [3] Institut Curie, Université PSL, Sorbonne Université, CNRS UMR 168, Laboratoire Physico Chimie

15 Curie,75005 Paris, France

16 [4] ARC Centre of Excellence in Advanced Molecular Imaging, Monash University, Australia; Biomedicine

17 Discovery Institute, Department of Biochemistry and Molecular Biology, Monash University, Clayton,

18 Australia

19 [5] Aix-Marseille Univ, CNRS, UMR 7051, Institut de Neurophysiopathologie (INP), Marseille, France

20 [6] Centre de Recherche en Cancérologie de Marseille (CRCM), INSERM, Institut Paoli-Calmettes, Aix

21 Marseille Univ, CNRS, 13009 Marseille, France

22 [7] Aix-Marseille Univ, INSERM, CNRS, Institut Paoli-Calmettes, CRCM, Marseille Protéomique, Marseille,

23 France

24 [8] Department of Living Matter, AMOLF, 1098 XG Amsterdam, The Netherlands

25 [9] Architecture et Fonction des Macromolécules Biologiques (AFMB), CNRS UMR7257, Aix Marseille Univ,

26 13009 Marseille, France

27 [10] Centre de Recherche en Cancérologie de Toulouse (CRCT), Inserm, Université Paul Sabatier-Toulouse

28 III, CNRS, 31037 Toulouse, France

29

30 [#] current affiliation: Institut Curie, Université PSL, Sorbonne Université, CNRS UMR 168, Laboratoire

31 Physico Chimie Curie,75005 Paris, France

32

33 *Corresponding authors:

34 Manos Mavrakis ; ORCID ID 0000-0002-7980-1841 ; manos.mavrakis@univ-amu.fr ; mailing address:

35 Institut Fresnel, Campus St Jérôme, 52 avenue Escadrille Normandie-Niemen, 13013 Marseille, France

36 Aurélie Bertin ; ORCID ID 0000-0002-3400-6887 ; aurelie.bertin@curie.fr ; mailing address: Laboratoire

37 Physico Chimie Curie, Institut Curie, 11 rue Pierre et Marie Curie, 75005 Paris, France

38 Gijsje H. Koenderink ; ORCID ID 0000-0002-7823-8807 ; G.H.Koenderink@tudelft.nl ; mailing address:

39 TU Delft, Faculty of Applied Sciences, Building 58, Van der Maasweg 9, 2629 HZ Delft, The Netherlands

40

41

42

43 **Running Title**

44 **Recombinant human septin octamers containing SEPT9**

Summary

Human septins in cells form hetero-octameric complexes containing the ubiquitously expressed SEPT9. Iv et al. describe the first-time isolation of recombinant human septin octamers with distinct SEPT9 isoforms. Reconstitution studies show that octamers with either a long or a short SEPT9 isoform form higher-order filament assemblies and directly bind and cross-link actin filaments.

Abstract

Septin GTP-binding proteins contribute essential biological functions that range from the establishment of cell polarity to animal tissue morphogenesis. Human septins in cells form hetero-octameric septin complexes containing the ubiquitously expressed SEPT9. Despite the established role of SEPT9 in mammalian development and human pathophysiology, biochemical and biophysical studies have relied on monomeric SEPT9 thus not recapitulating its native assembly into hetero-octameric complexes. We established a protocol that enabled the first-time isolation of recombinant human septin octamers containing distinct SEPT9 isoforms. A combination of biochemical and biophysical assays confirmed the octameric nature of the isolated complexes in solution. Reconstitution studies showed that octamers with either a long or a short SEPT9 isoform form filament assemblies, and can directly bind and cross-link actin filaments, raising the possibility that septin-decorated actin structures in cells reflect direct actin-septin interactions. Recombinant SEPT9-containing octamers will make it possible to design cell-free assays to dissect the complex interactions of septins with cell membranes and the actin/microtubule cytoskeleton.

2

Introduction

Septins constitute a family of GTP-binding proteins conserved from algae and protists to mammals (Cao et al., 2007; Momany et al., 2008; Nishihama et al., 2011; Pan et al., 2007). Septins are involved in a wide range of biological processes, from the establishment of cell polarity and cell division to cell-cell adhesion, cell motility, animal tissue morphogenesis and infection (Fung et al., 2014; Marquardt et al., 2019; Mostowy and Cossart, 2012; Weirich et al., 2008). In human pathophysiology, a role of septins has been established in neuropathies, infertility and tumorigenesis (Dolat et al., 2014a; Montagna et al., 2015). Despite their essential roles, how human septins organize and function in cells remains much more poorly understood than for budding yeast, in which septins were first discovered (Hartwell, 1971; Hartwell et al., 1970). Mammalian septins are thought to associate with cell membranes (Akil et al., 2016; Bridges et al., 2016; Damalio et al., 2013; Dolat and Spiliotis, 2016; Omrane et al., 2019; Tanaka-Takiguchi et al., 2009; Zhang et al., 1999) like their yeast counterparts (Bertin et al., 2010; Bridges et al., 2016; Bridges et al., 2014; Casamayor and Snyder, 2003). Unlike budding yeast septins, mammalian septins localize extensively to actin and microtubules in cells, for example to the ingressing cytokinetic ring in dividing cells (Estey et al., 2010; Joo et al., 2007; Kim et al., 2011; Kinoshita et al., 1997; Surka et al., 2002), stress fibres in interphase cells (Calvo et al., 2015; Connolly et al., 2011; Dolat et al., 2014b; Joo et al., 2007; Kim et al., 2011; Kinoshita et al., 2002; Kinoshita et al., 1997; Liu et al., 2014; Surka et al., 2002; Verdier-Pinard et al., 2017; Xie et al., 1999; Zhang et al., 1999), and to interphase, mitotic spindle, and intercellular bridge microtubules (Bowen et al., 2011; Nagata et al., 2004; Nagata et al., 2003; Spiliotis et al., 2008; Spiliotis et al., 2005; Surka et al., 2002; Verdier-Pinard et al., 2017). Mammalian septin association with membranes as well as with the actin and microtubule cytoskeleton has made it difficult to dissect how they function, and at the same time raises the intriguing possibility that septins mediate cytoskeleton-membrane cross-talk.

Studies of native and recombinant septins isolated from budding yeast (Bertin et al., 2008; Farkasovsky et al., 2005; Frazier et al., 1998; Garcia et al., 2011; Versele and Thorner, 2004), *Drosophila* (Field et al., 1996; Huijbregts et al., 2009; Mavrakis et al., 2014), *C. elegans* (John et al., 2007), and mammalian cell lines and tissues (Hsu et al., 1998; Kim et al., 2011; Kinoshita et al., 2002; Sellin et al., 2011; Sirajuddin et al., 2007) have established that septins form heteromeric complexes, with each septin present in two copies, forming a palindrome. Phylogenetic analysis has classified human septins in four homology groups, namely the SEPT2 group (SEPT1, 2, 4, and 5), SEPT6 group (SEPT6, 8, 10, 11, and 14), SEPT7 group (SEPT7), and SEPT3 group (SEPT3, 9, and 12) (Kinoshita, 2003) (see Materials and methods for nomenclature). Native human septins isolated from cells exist in the form of stable hexamers and octamers (Kim et al., 2011; Sellin et al., 2011; Sellin et al., 2014). Hexamers are composed of septins from the SEPT2, SEPT6, SEPT7 groups, while octamers contain additional septins from the SEPT3 group (Fig. 1 A).

113   A well-documented feature of septins is that purified septin heteromeric complexes self-
114   assemble into filaments (Valadares et al., 2017). Whether all native septin pools are
115   filamentous, and how septin function is linked to the relative distributions of hexamers
116   and octamers and their polymerization capacity within cells are not known. The most
117   convincing evidence that septins form filaments *in vivo*, and that septin function depends
118   on their ability to assemble into filaments, comes from budding yeast (Bertin et al., 2012;
119   Byers and Goetsch, 1976; McMurray et al., 2011; Ong et al., 2014; Rodal et al., 2005).
120   A powerful tool for studying septin assembly and function has been the use of
121   recombinant septin complexes. Earlier studies using recombinant mammalian septin
122   complexes have combined septins from two or more species, most likely for pragmatic
123   reasons. Mouse SEPT2 was combined with human SEPT6 and SEPT7 (Kinoshita et al.,
124   2002; Mavrakis et al., 2014; Sirajuddin et al., 2007), or with human SEPT6, SEPT7 and
125   SEPT3 (DeRose et al., 2020), and mouse SEPT2 was also combined with human SEPT6
126   and rat SEPT7 (Bai et al., 2013). Furthermore, the longest SEPT7 isoform (UNIPROTKB
127   identifier Q1681-1) was originally annotated with its N-terminus missing 19 residues
128   (Macara et al., 2002). There are currently no studies showing whether these specific
129   species-related differences affect septin function. Still, taking into account that these
130   differences lie in exposed residues in the very N- or/and C-terminal extensions (Fig. 1 A,
131   B), or within exposed loops in the GTP-binding domain, and given how poorly we
132   understand the factors that impact animal septin assembly and function, there is a clear
133   need to produce septin complexes with full-length septins from one species, notably
134   human septin octamers containing SEPT2, SEPT6, SEPT7, and SEPT9.
135   SEPT9 is the only septin from the SEPT3 group whose expression is ubiquitous across
136   human tissues, with SEPT3 and SEPT12 being neuron- and testis-specific, respectively
137   (Cao et al., 2007; Connolly et al., 2011; Hall et al., 2005). *Sept9* gene knockout in mice is
138   embryonic lethal (Fuchtbauer et al., 2011), and a large body of literature has implicated
139   SEPT9 in diverse human cancers (Dolat et al., 2014a; Montagna et al., 2015). There are
140   five SEPT9 isoforms (SEPT9_i) differing in the length and composition of the N-terminal
141   extension preceding the GTP-binding domain (Connolly et al., 2014; McIlhatton et al.,
142   2001) (Fig. 1 B). Distinct SEPT9 isoforms can have different functions, as reported for
143   cytokinesis and cancer cell migration (Estey et al., 2010; Verdier-Pinard et al., 2017).
144   Despite its importance in mammalian development and human pathophysiology,
145   biochemical and biophysical studies of SEPT9 have been limited to the use of monomeric
146   SEPT9 and fragments thereof (Bai et al., 2013; Dolat et al., 2014b; Nakos et al., 2019;
147   Smith et al., 2015), thus not recapitulating its native assembly into hetero-octameric
148   complexes (Sellin et al., 2011; Sellin et al., 2014). Multiple studies have documented
149   promiscuity in septin-septin interactions in the absence of their physiologically relevant
150   binding partners, affecting the availability of specific structural elements for interactions
151   with other septins or interacting proteins (Castro et al., 2020; Valadares et al., 2017). The
152   necessity to study septins in the context of their native heteromeric complexes is
153   highlighted by the increasing number of structural studies of the factors governing the

154 molecular specificity that determines the correct pairing of septins during complex
155 assembly (Kumagai et al., 2019; Rosa et al., 2020; Sala et al., 2016).
156 The N-terminal extension in the long SEPT9 isoforms (SEPT9_i1, SEPT9_i2 and
157 SEPT9_i3) is of considerable size (~27-kDa, i.e. three-quarters of the size of the GTP-
158 binding domain) making these isoforms the longest, in terms of the number of residues,
159 of all human septins. Given that the long SEPT9 isoforms differ only in the composition
160 of their N-terminal 25, 18 and 7 residues, respectively (Fig. 1 B), it is intriguing that they
161 all associate with actin stress fibres in cells, whereas only SEPT9_i1 associates with
162 microtubules (Nagata et al., 2004; Nagata et al., 2003; Surka et al., 2002). Different cell
163 types express different sets of SEPT9 isoforms, with some cell types expressing specific
164 long SEPT9 isoforms, and others lacking altogether long SEPT9 isoforms (Burrows et al.,
165 2003; Sellin et al., 2014; Verdier-Pinard et al., 2017). Hereditary neuralgic amyotrophy
166 (HNA), a rare neuropathy, has been mapped to missense mutations and duplications in
167 the large N-terminal extension shared by the long SEPT9 isoforms (Collie et al., 2010;
168 Hannibal et al., 2009; Kuhlenbaumer et al., 2005; Landsverk et al., 2009). Understanding
169 SEPT9 function thus necessitates the isolation of recombinant septin octamers bearing
170 distinct SEPT9 isoforms.
171 To enable studies of SEPT9 function in the context of its physiological assembly into
172 hetero-octamers, we established a protocol that enabled, for the first time, the isolation of
173 recombinant human septin octamers containing distinct SEPT9 isoforms (Fig. 1 B). A
174 combination of biochemical and biophysical assays confirmed the octameric nature of the
175 isolated octamers in solution, and also provided evidence for SEPT2 and SEPT9
176 occupying the end and central positions in the octamer. Fluorescence and electron
177 microscopy showed that recombinant octamers containing either a long or a short SEPT9
178 isoform form higher-order filament assemblies. As a first step towards the reconstitution
179 of recombinant SEPT9-containing octamers with known physiological interactors, we
180 examined their interactions with actin filaments. Reconstitution studies showed that
181 octamers with either a long or a short SEPT9 isoform directly bind and cross-link actin
182 filaments, raising the possibility that septin-decorated actin bundles in cells reflect direct
183 actin-septin interactions. Biochemical and biophysical reconstitution studies of
184 recombinant octamers containing distinct SEPT9 isoforms with physiological septin
185 interactors, such as membranes and microtubules, promise to provide a powerful
186 complementary approach to cell and animal model studies of septin organization and
187 function.
188
189 **Results and discussion**
190
191 **A two-tag purification scheme yields stoichiometric recombinant human septin**
192 **octamers containing distinct SEPT9 isoforms**
193 To isolate octamers containing either a long SEPT9 isoform, in particular SEPT9_i1 and
194 SEPT9_i3, or octamers containing a short SEPT9 isoform, SEPT9_i5 (Fig. 1 B), we

195 combined the pET-MCN (pET Multi-Cloning and expressioN) series as a septin co-
196 expression system (Diebold et al., 2011) with a two-tag purification scheme. We used two
197 bicistronic vectors: one vector co-expressing SEPT2 and SEPT6, the other one SEPT7
198 and SEPT9_i (Fig. S1 A). To minimally perturb septin complex assembly, and interactions
199 with other proteins or membranes, we chose small (1 kDa) tags, a hexahistidine (His$_6$)
200 tag and the eight amino-acid Strep-tag II (Fig. S1 B). To isolate octamers, we tagged the
201 N-terminus of the end subunit, SEPT2, with a tobacco etch virus (TEV) protease-
202 cleavable His$_6$-tag, and the C-terminus of the central subunit, SEPT9_i, with a TEV-
203 cleavable Strep-tag. The use of a Strep-Tactin affinity column to capture Strep-tagged
204 SEPT9_i-containing complexes, followed by a nickel affinity column to retain the
205 SEPT9_i-containing complexes that also bear His$_6$-tagged SEPT2, is expected to isolate
206 SEPT2-SEPT6-SEPT7-SEPT9 complexes (Fig. 1 C). We used this purification scheme
207 to isolate both nonfluorescent septin complexes and fluorescent septin complexes
208 containing SEPT2 with its C-terminus fused to monomeric superfolder GFP (msfGFP)
209 (Costantini et al., 2012; Cranfill et al., 2016; Pedelacq et al., 2006; Zacharias et al., 2002).
210 Indeed, SDS-PAGE analysis of the purification of human septin complexes containing
211 SEPT9_i1 (octamers-9_i1), SEPT9_i3 (octamers-9_i3), or SEPT9_i5 (octamers-9_i5),
212 followed by Coomassie staining, showed that our purification scheme succeeded to
213 isolate SEPT2-SEPT6-SEPT7-SEPT9 complexes (Fig. 1 D). The assignment of the
214 bands to the different septins was based on Western blot analysis and mass
215 spectrometry. Western blots (Fig. S1 F), tryptic peptide coverage and pseudo-absolute
216 quantitation of the mol fractions of proteins in our preps by mass spectrometry (Fig. S1 G
217 and H) showed that the isolated complexes were >97% pure, intact and with SEPT2,
218 SEPT6, SEPT7, SEPT9 in a 1:1:1:1 stoichiometry. We note that inverting the two
219 columns, using batch affinity resins instead of prepacked columns, or combining
220 prepacked columns and resins, all provided similar results (Fig. S 1 C-E).
221 Given that the purification scheme *per se* cannot distinguish between tetramers and
222 octamers, we sought to determine if the isolated SEPT2-SEPT6-SEPT7-SEPT9
223 complexes were composed of tetramers or/and octamers by blue native PAGE followed
224 by Coomassie staining (Fig. 1 E). For comparison, we included recombinant human
225 SEPT2-, SEPT6-, SEPT7-containing hexamers that we isolated with the same purification
226 protocol (Fig. S1 A). Blue native PAGE has been a powerful tool in detecting the presence
227 and relative distributions of endogenous septin complexes in cell lysates, and is able to
228 resolve septin tetramers from hexamers and octamers (Sellin et al., 2014). Native PAGE
229 analysis of our hexamer and octamer preps showed bands that were in line with the
230 presence of hexamers for the hexamer prep and octamers for the octamer preps, while
231 providing no evidence for the presence of tetramers, suggesting that the latter either do
232 not form, or they do so transiently. Our findings are consistent with SEPT9 being present
233 in the form of stable octamers in cells (Sellin et al., 2011; Sellin et al., 2014).
234 To further corroborate the presence of a stable octameric population in our preps, we
235 turned to analytical ultracentrifugation sedimentation equilibrium assays, comparing side

6

236   by side hexamers and SEPT9_i5-containing octamers. Sedimentation equilibrium
237   experiments provide an experimental measure of the absolute mass of proteins in solution
238   (Taylor et al., 2015) and thus a powerful means of determining the species present in our
239   preps. The obtained molecular masses from such experiments were consistent with the
240   presence of hexamers for the hexamer preps, and the presence of octamers for the
241   octamer preps, without any detectable evidence for tetrameric complexes in the octamer
242   preps (Fig. 1 F). We complemented these assays with analytical ultracentrifugation
243   sedimentation velocity experiments comparing octamer-9_i1 and octamer-9_i3 preps
244   (Fig. 1 G). Sedimentation velocity assays measure the experimental sedimentation
245   coefficient of proteins in solution and are thus able to detect the presence of multiple
246   protein species. Sedimentation coefficients depend on the hydrodynamic properties of
247   proteins, and are directly proportional to their mass and translational diffusion coefficient,
248   the latter including the contribution of protein shape. To interpret the obtained
249   sedimentation coefficients and given the prediction of C-terminal coiled-coils for SEPT2,
250   SEPT6 and SEPT7 (de Almeida Marques et al., 2012; Low and Macara, 2006; Sala et
251   al., 2016) (Fig. 1 A, B), we used coiled-coil modeling and homology-modeling software to
252   build a model of the SEPT2-SEPT6-SEPT7-SEPT9-SEPT9-SEPT7-SEPT6-SEPT2
253   octamer (Fig. 1 H). We used this model structure together with the Svedberg equation
254   and the HullRad algorithm (Fleming and Fleming, 2018) which calculates hydrodynamic
255   properties of molecules from their structures, to obtain the theoretical diffusion coefficients
256   of octamers and tetramers, as well as their theoretical sedimentation coefficients (table in
257   Fig. 1 G, see Materials and methods for details). The experimental sedimentation
258   coefficients for octamers-9_i1 and octamers-9_i3 were in excellent agreement with the
259   ones estimated from the model structure, with the sedimentation coefficient distributions
260   again providing no evidence for the presence of tetramers that are expected to sediment
261   much more slowly (by ~ 3 S).

262

263   **Single particle electron microscopy analysis of recombinant septin octamers**
264   **reveals the flexibility of N- and C-terminal extensions, and provides evidence for**
265   **SEPT2 and SEPT9 occupying the end and central positions, respectively**
266   To visualize the isolated octamers, we employed single particle electron microscopy (EM)
267   of negative-stained octamer preps in a high salt buffer (300 mM KCl) to prevent septin
268   complexes from polymerizing. Low magnification EM images of negative-stained octamer
269   preps highlighted the rod-like appearance of the complexes (Fig. 2 A). Single particles in
270   such fields, typically ~3-4,000 particles, were computationally aligned and classified into
271   classes with distinct features (for example, orientation, curvature, or number of subunits).
272   Each class typically contained ~50-100 particles (see Materials and methods). Fig. 2 B
273   shows a gallery of class averages for octamers-9_i3. Each image is the average of all the
274   particles in a given class, and has an increased signal to noise ratio compared to the raw
275   images, which allows us to distinguish individual septin subunits within the octameric
276   complex. All class averages for octamers-9_i3 exhibited a characteristic rod shape,

277 similarly to recombinant human/mammalian septins (Mavrakis et al., 2016; Mendonca et
278 al., 2019; Sirajuddin et al., 2007) or septins isolated from mammalian cell lines and tissues
279 (Hsu et al., 1998; Kim et al., 2011; Kinoshita et al., 2002; Sellin et al., 2011; Soroor et al.,
280 2020), and in line with rod-shaped septin complexes from other species, including
281 budding yeast (Bertin et al., 2008; Frazier et al., 1998; Garcia et al., 2011; Taveneau et
282 al., 2020), *C. elegans* (John et al., 2007) and *Drosophila* (Akhmetova et al., 2015; Field
283 et al., 1996; Mavrakis et al., 2014). The class averages did not show additional densities
284 at their ends or along their sides, suggesting an intrinsic orientational flexibility in the
285 junction between the G domain and the coiled-coils of SEPT2, SEPT6 and SEPT7, whose
286 densities are averaged out in such analysis. Such flexibility for the coiled-coils, deduced
287 from the absence of electron density in the crystal structure of the SEPT2-SEPT6-SEPT7
288 trimer (Sirajuddin et al., 2007) and the absence of additional densities in single particle
289 EM of budding yeast, mammalian, *C.elegans* and *Drosophila* complexes (Bertin et al.,
290 2008; Garcia et al., 2011; John et al., 2007; Mavrakis et al., 2014; Mavrakis et al., 2016;
291 Mendonca et al., 2019; Taveneau et al., 2020), seems to be a general feature of septins.
292 Moreover, there was no density that could be assigned to the large (~27-kDa) N-terminus
293 of the long isoforms, in line with the absence of any secondary structure prediction for this
294 SEPT9 long isoform-specific domain (see Materials and methods).
295 Class averages of SEPT2-msfGFP octamers-9_i1 (Fig. 2 C) did display additional
296 densities at one or both ends of the rods (green arrowheads), indicating that the GFP-
297 tagged SEPT2 subunits occupy the termini of octamers. The same observation was made
298 with SEPT2-msfGFP-containing hexamers (Fig. 2 D). The fuzzy density of the C-terminal
299 GFP and its multiple positions around SEPT2 again point to a flexible hinge region
300 between the last helix of the G-domain (α6 helix, Fig. 1 H) and the coiled-coils of SEPT2
301 (Fig. 1A, B, H). Class averages of octamers-9_i1 incubated with anti-SEPT9 antibodies
302 exhibited additional fuzzy densities closest to the central subunits (Fig. 2 E, white arrows),
303 consistent with SEPT9 occupying the central positions in the octameric rods. Our
304 observations on the positioning of SEPT2 and SEPT9 in the isolated octamers are thus
305 consistent with recent studies on septin positioning in recombinant human hexamers
306 (Mendonca et al., 2019), recombinant SEPT3-containing octamers (DeRose et al., 2020)
307 and SEPT9-containing octamers isolated from cell lysates (Soroor et al., 2020) (Fig. 2 F).
308

Recombinant septin octamers harboring either SEPT9_i1, SEPT9_i3, or SEPT9_i5
polymerize into higher-order filament assemblies in solution
311 In addition to SEPT2 at the ends of octamers, whose presence is determinant for octamer
312 polymerization in solution, other structural elements such as the N- or C-terminal
313 extensions could also impact septin filament assembly (Bertin et al., 2010). To test the
314 effect of the SEPT9-specific N-terminal extension on septin polymerization in solution, we
315 compared octamers containing either a long or a short SEPT9 isoform. To this end,
316 octamers-9_i1, -9_i3 and -9_i5 were either dialyzed or diluted into a low-salt buffer (50
317 mM KCl). The resulting assemblies were observed with spinning disk fluorescence

318 microscopy on PLL-PEG passivated glass using SEPT2-msfGFP containing octamers
319 (Fig. 3 A-C), and examined at higher spatial resolution by negative-stain EM using
320 nonfluorescent or SEPT2-msfGFP containing octamers (Fig. 3 D-E). Both octamers with
321 a long or a short SEPT9 isoform polymerized into higher-order filament assemblies.
322 Fluorescence microscopy revealed a variety of assembly morphologies: optical
323 sectioning showed that all octamers assembled into interconnected and/or branched
324 networks of straight and curved filament bundles extending along 10-50 μm in the xy
325 plane and by 10-50 μm in z (Video 1 shows a representative z-stack, and Fig. 3 A-C show
326 maximum-intensity projections of z-stacks). Octamers could organize into straight
327 bundles (left panel in Fig. 3 B; Fig. 3 C), but also into what looked like highly convoluted
328 filamentous assemblies (Fig. 3 A; right panel in Fig. 3 B). Measurements of isolated septin
329 filament bundles in solution for octamers-9_i3 and -9_i5 (left panel in Fig. 3 B; Fig. 3 C)
330 showed that they could reach up to ~5-8 μm in length.
331 Negative-stain EM similarly revealed a variety of filamentous assemblies. Octamers-9_i1
332 could organize into isolated or interconnected straight or slightly curved bundles (Fig. 3
333 D, i-ii), and into networks of interconnected highly convoluted and ring-forming filament
334 bundles (Fig. 3 D, iii-v) corresponding to the similarly convoluted filamentous assemblies
335 in fluorescence microscopy (Fig. 3 A). Septin filament bundles were a few μm long and
336 ~50-150 nm in width (Fig. S2 E). High magnifications of regions within the filament
337 bundles (red-outlined insets in Fig. 3 D) revealed that bundles were made of single septin
338 filaments (blue arrowheads in Fig. 3 D and measurements of septin filament width in Fig.
339 S2 E) running parallel to each other, with septin filaments within bundles occasionally
340 looking paired (orange arrowheads in Fig. 3 D). Given the high density of filaments and
341 the 2D projection character of negative-stain EM, we cannot conclude if these are truly
342 paired filaments like budding yeast septin filament pairs (Bertin et al., 2008); if so, these
343 would have to be more tightly paired given their interfilament spacing (~2-3 nm). Septin
344 filament bundles exhibited a high degree of interconnectivity, with a given bundle often
345 showing splayed ends that could connect to one or more different bundles, or with septin
346 filaments forming meshes (Fig. 3 D, v). We speculate that the exposed, flexible coiled-
347 coil-containing C-terminal extensions, and potentially the long N-terminal extensions of
348 SEPT9, drive the interconnections in the higher-order assemblies we observe. Octamers-
349 9_i3 also formed filament bundles (Fig. 3 E, i) and *bona fide* paired filaments with
350 narrower interfilament spacing (~2-3 nm) than the one observed for budding yeast septin
351 filament pairs in solution (~10 nm) (Bertin et al., 2008) (Fig. 3 E, ii). Octamers-9_i3
352 additionally formed wheel-like structures associating with the bundles (Fig. 3 E, i, green
353 arrowheads). These wheels had a diameter of 20-30 nm and could correspond to two or
354 three octamer rods connected end to end; the interior of the wheels appeared to contain
355 electron density. Very similar-looking wheels of similar dimensions have been reported
356 for budding yeast Shs1-containing octamers, with the electron density in their interior
357 attributed to the C-terminal coiled-coils stabilizing these structures (Garcia et al., 2011;
358 Taveneau et al., 2020). Our combined observations from fluorescence and electron

9

359 microscopy show that recombinant octamers with either a long or a short SEPT9 isoform
360 form higher-order filament assemblies, and are consistent with studies of SEPT9-
361 containing octamers isolated from cell lysates (Soroor et al., 2020).
362 For comparison, we examined human septin hexamers, mammalian septin hexamers
363 (containing mouse SEPT2, human SEPT6 and human SEPT7ΔN19), and *Drosophila*
364 hexamers whose polymerization was characterized previously (Mavrakis et al., 2014;
365 Mavrakis et al., 2016). Fluorescence microscopy and negative-stain EM of human,
366 mammalian and *Drosophila* hexamers in a low-salt buffer (Fig. S2 A-D) showed that
367 human and mammalian hexamers organized in a very similar manner into straight and
368 curved filament bundles made of single and possibly paired septin filaments (Fig. S2 C,
369 D; Fig. S2 E). *Drosophila* hexamers organized in characteristic needle-like bundles, as
370 reported previously (Mavrakis et al., 2014; Mavrakis et al., 2016), which were not as
371 heavily interconnected as their human counterparts. Human hexamer- and octamer-
372 bundles displayed similar lengths and widths (Fig. S2 E, see legend for median values).
373 The observation of such a large variety in the morphologies of filament assemblies in
374 solution could result from several factors. In this study we examined septin assembly
375 using recombinant octamers bound to the endogenous GDP/GTP in the bacterial
376 cytoplasm, without the exogenous addition of nucleotide during cell lysis or post-
377 purification; it is conceivable that regulation of the GDP/GTP state of septins in cells
378 regulates their higher-order assembly (Weems and McMurray, 2017). A further important
379 element is that interactions of septins with membranes, accessory proteins, or the
380 actin/microtubule cytoskeleton could influence their assembly in cells. Our observations
381 lead us to speculate that, in the absence of any other interacting surface or protein,
382 higher-order septin assembly is dominated by the exposed, flexible coiled-coil-containing
383 C-terminal extensions, resulting in the high plasticity and polymorphism we observe. The
384 filamentous assemblies we observe in solution could reflect higher-order septin
385 filamentous assemblies that have been observed in the cytosol of cells upon perturbation
386 of interacting partners, for example, upon disruption of actin stress fibres (Joo et al., 2007;
387 Kim et al., 2011; Kinoshita et al., 2002; Kinoshita et al., 1997; Xie et al., 1999).
388

389 **Recombinant octamers-9_i1, octamers-9_i3 and octamers-9_i5 bind and cross-link**
390 **actin filaments in solution**
391 Septins are thought to interact with actin filaments either indirectly via myosin-II (Joo et
392 al., 2007), or directly. The possibility of direct interactions between septin hexamers and
393 actin filaments was raised by reconstitution assays showing that recombinant mammalian
394 and *Drosophila* hexamers bind and cross-link actin filaments into bundles (Mavrakis et
395 al., 2014). Given that in cells both long isoforms, SEPT9_i1 and SEPT9_i3, and the short
396 isoform SEPT9_i5 associate with the actin cytoskeleton (Connolly et al., 2011; Dolat et
397 al., 2014b; Kim et al., 2011; Surka et al., 2002; Verdier-Pinard et al., 2017), we sought to
398 test if recombinant octamers-9_i1, -9_i3 and -9_i5 have the capacity to directly bind and

10

399 cross-link actin filaments, as hexamers do, and if so, whether the presence of a specific
400 SEPT9 isoform makes any difference.

401 To this end, we used spinning disk fluorescence microscopy to image dilute solutions (1
402 μM) of single actin filaments on PLL-PEG passivated glass, after spontaneous
403 polymerization of purified rabbit muscle G-actin in the presence or absence of
404 nonfluorescent or SEPT2-msfGFP-containing octamers-9_i1, -9_i3 and -9_i5 (Fig. 4 A-
405 E). In the absence of octamers, fluorescence microscopy showed isolated fluctuating
406 single actin filaments, as expected (Fig. 4 A and Video 2). In the presence of 0.3 μM
407 SEPT2-msfGFP-containing octamers-9_i1 (Fig. 4 C), octamers-9_i3 (Fig. 4 D), or
408 octamers-9_i5 (Fig. 4 E), fluorescence microscopy revealed actin filaments cross-linked
409 into straight and curved bundles, in a very similar manner for all three types of octamers,
410 and very similarly to cross-linking induced by human, mammalian and *Drosophila*
411 hexamers (Fig. S3 A-C and (Mavrakis et al., 2014)). Actin filament cross-linking was
412 observed for septin concentrations of 20-30 nM and above, with identical results obtained
413 with nonfluorescent septins (data not shown). The images shown in Fig. 4 C-E were
414 captured typically a few hours into actin polymerization or after overnight incubation, and
415 show the coexistence of straight and curved actin filament bundles, either isolated ones
416 or bundles connected to each other forming networks. Thicker actin bundles,
417 corresponding to a brighter signal in the actin channel, fluctuated very little, suggesting
418 that they were rigid, whereas thinner actin bundles and single actin filaments, emanating
419 from the ends or the sides of bundles, or connecting neighboring bundles, were freely
420 fluctuating (Video 3). Septins systematically colocalized with the actin bundles, indicative
421 of their actin filament cross-linking activity (right panels in Fig. 4 C-E depict insets of
422 selected red-outlined regions on the left). Saturating the actin and septin channels to bring
423 out features with weaker signals, notably single actin filaments (arrowheads in the actin
424 channel in Fig. 4 C-E), revealed that septins localized only to actin bundles and not to
425 single actin filaments, suggesting cooperativity in septin-actin binding. Such cooperativity
426 has also been reported for other actin filament cross-linkers (Winkelman et al., 2016). The
427 similarities in the actin filament cross-linking capacities of human octamers-9_i1, -9_i3
428 and -9_i5 and human hexamers raise the possibility that SEPT9, in the context of an
429 octameric complex, does not contribute to actin filament cross-linking, but we cannot
430 exclude such a contribution (Dolat et al., 2014b; Smith et al., 2015). In the latter case, the
431 contribution of SEPT9 to actin filament cross-linking seems to be indistinguishable from
432 the one of the other septins in the complex. Our observations raise the possibility that
433 septin-decorated actin structures such as stress fibres and the cytokinetic ring reflect
434 direct interactions between actin filaments and hexameric or/and octameric septin
435 complexes.

436 In summary, our study describes the first isolation and characterization of recombinant
437 human SEPT2-SEPT6-SEPT7-SEPT9-SEPT9-SEPT7-SEPT6-SEPT2 octamers
438 containing distinct long or short SEPT9 isoforms. The employed two-tag purification
439 scheme is rapid, taking one full day starting from bacteria lysis, works with prepacked

11

440 columns, batch resins, or combinations thereof thus providing flexibility, and yields ~1-3
441 mg of purified octamers (a few hundreds of microliters in the micromolar concentration
442 range), enabling biochemical and biophysical reconstitution studies at physiological
443 septin concentrations. A combination of biochemical and biophysical assays confirmed
444 the octameric nature of the isolated complexes in solution, and also provided evidence
445 for SEPT2 and SEPT9 occupying the end and central positions in the octamer.
446 Recombinant octamers with either a long or a short SEPT9 isoform were competent for
447 polymerization in solution, and they all shared the capacity to cross-link actin filaments.
448 Given the importance of SEPT9 in mammalian physiology and disease, the isolation of
449 recombinant human septin octamers bearing distinct SEPT9 isoforms will facilitate
450 studies of SEPT9 in the physiological context of its assembly into hetero-octamers.
451 Septins engage in multiple interactions, making it difficult to dissect their function in the
452 complex environment of the cell. Cell-free reconstitution studies with SEPT9-containing
453 octamers and candidate interacting partners thus provide a powerful complementary
454 approach to cellular and animal model studies for exploring human septin function.
455
456 **Figure legends**
457
458 Figure 1. **Isolation and characterization of recombinant human octamers containing**
459 **distinct SEPT9 isoforms. (A-B)** Schematic representation of a mammalian septin
460 showing the conserved GTP-binding (G) domain flanked by N- and C-terminal extensions.
461 There is experimental evidence that the N-terminal extension, at least for some septins,
462 is intrinsically disordered (Garcia et al., 2006). With the exception of SEPT3 group
463 septins, the C-terminal extension is predicted to contain a coiled-coil (A). Schematics in
464 (B) depict the human septins used in this study, their size indicated by the very C-terminal
465 residue number. Residue numbers at the start and end of the G-domains correspond to
466 the start of the $\alpha 0$ helices and the end of the $\alpha 6$ helices, respectively. Residue numbers
467 right after the isoform-specific sequences for SEPT9_i1 and SEPT9_i3 indicate the start
468 of their shared long N-terminal extension. The last 28 residues of this extension constitute
469 the N-terminal extension of the short isoform, SEPT9_i5. Color-coded spheres depicting
470 the different subunits throughout the manuscript are shown next to the respective septins.
471 The freehand line preceding the SEPT9 G domain of the long isoforms depicts their large
472 N-terminal extension. **(C)** Schematic overview of the two-tag affinity purification scheme
473 for isolating stoichiometric SEPT9-containing octamers. Upon septin co-expression in the
474 bacteria cytoplasm, septins are expected to form stable hexamers and octamers (Kim et
475 al., 2011; Sellin et al., 2011; Sellin et al., 2014). Other hypothetical homo- and hetero-
476 subcomplexes could also form (Kim et al., 2012; Rosa et al., 2020; Valadares et al., 2017).
477 A first Strep-tag affinity column isolates all Strep-tagged SEPT9 complexes ("S" for Strep-
478 tag). A second nickel affinity step further isolates His_6-tagged SEPT2-containing
479 complexes ("H" for His_6-tag), thus purifying SEPT2-SEPT6-SEPT7-SEPT9 complexes.
480 **(D)** SDS-PAGE analysis of the purification of human septin octamers containing

481 SEPT9_i1 (left, 8mer-9_i1), SEPT9_i3 (middle, 8mer-9_i3) and SEPT9_i5 (right, 8mer-
482 9_i5). Coomassie-stained gels show fractions eluting from the Strep-tag affinity column,
483 from the nickel affinity column and after the final dialysis step. Molecular weight markers
484 are shown on the left; the same markers were used in all gels. The 8mer-9_i1 and 8mer-
485 9_i3 complexes shown are nonfluorescent, whereas the 8mer-9_i5 complexes shown
486 contain msfGFP-tagged SEPT2. The identification of the bands corresponding to the
487 different septins was based on mass spectrometry and Western blot analysis (Fig. S1 F).
488 See Materials and methods for the theoretical and apparent molecular masses. **(E)**
489 Purified recombinant hexamers (6mer), 8mer-9_i1 and 8mer-9_i3 analyzed by blue native
490 PAGE, followed by Coomassie-staining. Molecular weight markers are shown on the left.
491 The apparent molecular masses for the recombinant 6mer and 8mer-9_i1 and -9i_3 are
492 in line with the molecular masses of native hexamers and octamers isolated from human
493 cell lysates (Sellin et al., 2014) (see also Materials and methods). The asterisk points to
494 the presence of presumed septin monomers/dimers (Sellin et al., 2014). **(F and G)**
495 Analytical ultracentrifugation of recombinant septin complexes. Sedimentation equilibrium
496 experiments (F) of 1.5 mg.mL^{-1} of 6mer (left) and 8mer-9_i5 (right) at 11,000 rpm and
497 4°C. The filled circle symbols show the experimental radial concentration distribution at
498 sedimentation equilibrium and the solid lines represent the best fit curves with the single-
499 ideal species model. The residuals representing the variation between the experimental
500 data and those generated by the fit are shown above the respective curves. The obtained
501 experimental molecular masses are indicated in the table below the curves. (G) shows
502 the sedimentation coefficient distributions *c(s)* of 0.3 mg.mL^{-1} 8mer-9_i3 (dark line) and
503 of 0.5 mg.mL^{-1} 8mer-9_i1 (dashed line) obtained from sedimentation velocity experiments
504 at 40,000 rpm and 20°C. The experimental sedimentation coefficients $s_{20,w}$ obtained are
505 indicated in the table below the curves. **(H)** Model of a human SEPT2-SEPT6-SEPT7-
506 SEPT9-SEPT9-SEPT7-SEPT6-SEPT2 octamer built using coiled-coil- and homology-
507 modelling software (see Materials and methods for details). An *en face* view (left) and a
508 side view after a 90° rotation (right) are shown. Coiled-coils are shown to extend along
509 the same axis as the α6 helix (arrow). The generated model was used to calculate the
510 theoretical translational diffusion coefficient, *D* (cm^2.s^{-1}), and the latter to further calculate
511 its theoretical sedimentation coefficient for comparison with the experimentally obtained
512 one (table in G) (see Materials and methods for details).

513

514 Figure 2. **Electron microscopy analysis of recombinant SEPT9-containing**
515 **octamers. (A)** Negative-stain EM image of recombinant 8mer-9_i1 at 25 nM in a high salt
516 buffer (300 mM KCl) showing the rod-like appearance of the complexes. **(B-E)** Single
517 particle EM analysis of recombinant septin complexes. Each panel shows a gallery of
518 representative class averages (~100 particles each) derived from the processing of
519 ~3,000-4,000 particles from micrographs of negative-stained complexes, as in (A) (see
520 Materials and methods for details). All class averages for 8mer-9_i3 complexes (B)
521 exhibited a rod shape with no evidence of additional densities at their ends or along their

522 sides, consistent with a high degree of flexibility for the coiled-coils of SEPT2, SEPT6 and
523 SEPT7, and in line with the absence of secondary structure prediction for the large (27-
524 kDa) N-terminus of the long SEPT9 isoforms. Class averages of SEPT2-msfGFP 8mer-
525 9_i1 (C) and of SEPT2-msfGFP 6mer (D) displayed additional densities at one or both
526 ends of the rods (green arrowheads), indicating that SEPT2 occupies the termini of 6mer
527 and 8mer. The fuzzy density of the C-terminal GFP and its multiple positions around the
528 end subunit suggest an intrinsic orientational flexibility in the junction between the G
529 domain and the coiled-coils of SEPT2. Class averages of 8mer-9_i1 incubated with anti-
530 SEPT9 antibodies (E) exhibited additional fuzzy densities closest to the center subunits
531 (white arrows), consistent with SEPT9 occupying the central positions in the octameric
532 rods. **(F)** shows the juxtaposition of the model of the octamer (Fig. 1 H) to a high
533 magnification class average image of an octamer from (B). All septin complexes shown
534 contain full-length, human septins apart from (B) which depicts an example of mammalian
535 septin octamers-9i3 containing mouse SEPT2-, human SEPT6-, human SEPT7ΔN19 and
536 human SEPT9_i3 (see Materials and methods).

537

538 Figure 3. *In vitro* **reconstitution of septin polymerization in solution using**
539 **recombinant septin octamers with distinct SEPT9 isoforms. (A-C)** Representative
540 spinning disk fluorescence images of higher-order filament assemblies upon
541 polymerization of 8mer-9_i1 (A), 8mer-9_i3 (B) and 8mer-9_i5 (C) after dilution into low
542 salt conditions (50 mM KCl) at the indicated final octamer concentration. Two examples
543 are shown for each. All images shown are maximum-intensity projections and use an
544 inverted grayscale. **(D)** Negative-stain EM images of higher-order filament assemblies
545 upon polymerization of 8mer-9_i1 at low salt (50 mM KCl). 8mer-9_i1 were polymerized
546 at 1 μM (D, i, ii) or 0.2 μM (D, iii-v) final octamer concentration. The insets show
547 magnifications of selected regions of interest (dashed rectangles in red), and highlight
548 single septin filaments (blue arrowheads), possibly paired septin filaments (orange
549 arrowheads), and splayed filament bundles (v). **(E)** Negative-stain EM images of higher-
550 order filament assemblies upon polymerization of 8mer-9_i3 at low salt (50 mM KCl).
551 8mer-9_i3 were polymerized at 0.2 μM final octamer concentration. The insets show
552 magnifications of selected regions of interest (dashed rectangles in red), and highlight
553 single septin filaments (blue arrowheads), paired septin filaments (orange arrowheads),
554 and wheel-like structures whose perimeter corresponds to two or three octamers
555 connected end to end (green arrowheads). All septin complexes shown contain full-
556 length, human septins apart from the left panel in (E) which depicts an example of
557 mammalian septin octamers-9i3 containing mouse SEPT2-, human SEPT6-, human
558 SEPT7ΔN19 and human SEPT9_i3 (see Materials and methods).

559

560 Figure 4. *In vitro* **reconstitution of actin filament cross-linking by recombinant**
561 **human septin octamers with distinct SEPT9 isoforms. (A-B)** Representative spinning
562 disk fluorescence images of reconstituted, fluctuating single actin filaments (A) upon

563   spontaneous polymerization of G-actin at 1 μM on PLL-PEG-passivated glass in a flow
564   chamber constructed as shown in (B) (see Materials and methods for details). Actin
565   filaments are visualized by including AlexaFluor568-conjugated phalloidin during
566   polymerization. The time lapse sequence containing the still image shown on the left
567   panel of (A) is shown in Video 2. **(C-E)** Representative spinning disk fluorescence images
568   of reconstituted actin filaments, prepared as in (A), and polymerized in the presence of
569   8mer-9_i1 (C), 8mer-9_i3 (D), or 8mer-9_i5 (E). Actin filaments are visualized with
570   AlexaFluor568-conjugated phalloidin, and septins with SEPT2-msfGFP. Two examples
571   of large fields of view are shown for each, depicting the similar cross-linking of actin
572   filaments into actin filament bundles in the presence of all three types of octamers; only
573   actin labeling is shown. A time lapse sequence containing the still image shown on the
574   right panel of (C) is shown in Video 3. Insets on the right side of each panel show higher
575   magnifications of selected regions of interest on the left (dashed squares in red). Two
576   regions of interest (i, ii) are shown in each case, depicting both the actin (top row) and
577   septin (bottom row) signals. For each inset, actin and septin signals are shown in
578   duplicates: the first set shows the raw signals without any saturation, whereas the second
579   set, adjacent to the first one, shows both actin and septin signals after deliberate contrast
580   enhancement. The contrast-enhanced images in the actin channel saturate the actin
581   bundles, while bringing out weaker-intensity single actin filaments (black arrowheads).
582   The respective contrast-enhanced images in the septin channel show the presence of
583   septins in actin bundles, but their absence from single actin filaments. Scale bars in all
584   large fields of views, 10 μm. Scale bars in all insets, 5 μm. All images shown use an
585   inverted grayscale.
586
587   ## Materials and methods
588
589   ### Plasmids and cloning
590   We refer to the mammalian septin protein products as SEPT2, SEPT6, SEPT7, and
591   SEPT9 (SEPT9_i to denote isoforms; the longest isoform being i1, the next longest i2,
592   and so on), nonitalicized and with all letters capitalized, according to the mammalian
593   septin nomenclature established by (Hall et al., 2008; Macara et al., 2002). Human septin
594   gene symbols are italicized with all capital letters, and mouse septin gene symbols
595   italicized with their first letter capitalized. Mouse SEPT2, human SEPT6 and human
596   SEPT7ΔN19 cDNAs were originally obtained from A. Wittinghofer (Max Planck Institute
597   of Molecular Physiology, Germany) and used for the expression and purification of
598   recombinant mammalian SEPT2-, SEPT6-, SEPT7-containing hexamers bearing TEV-
599   cleavable His$_6$-, N-terminally-tagged mouse SEPT2, human SEPT6 and noncleavable
600   Strep-tag-II-, C-terminally-tagged human SEPT7ΔN19 (Fig. S2 D and Fig. S3 C)
601   (Mavrakis et al., 2014). Human SEPT9_i1 cDNA was a gift from C. Montagna (Albert
602   Einstein College of Medicine, USA). Human SEPT9_i3 cDNA was a gift from W. Trimble
603   (University of Toronto, Canada). Both human SEPT9_i1 and SEPT9_i3cDNAs have a

604 valine at position 576 for SEPT9_i1 and 558 for SEPT9_i3 instead of a methionine,
605 compared to the respective sequences in UNIPROTKB (identifiers Q9UHD8-1 and
606 Q9UHD8-2); a valine in that position is found in several human clones and many other
607 primates suggesting this is a polymorphism. We used the pET-MCN vectors pnEA-vH
608 (pET15b backbone) and pnCS (pCDF-DuET backbone) for subcloning (Diebold et al.,
609 2011).
610 Building on our cloning strategy for generating hexamers and with the plasmids available
611 at the time (Mavrakis et al., 2014; Mavrakis et al., 2016), we generated initially a
612 bicistronic pnEA-vH vector for co-expression of TEV-cleavable His$_6$-, N-terminally-tagged
613 mouse SEPT2 and human SEPT6, and a bicistronic pnCS vector for co-expression of
614 human SEPT7ΔN19 and noncleavable Strep-tag-II-, C-terminally-tagged human
615 SEPT9_i3. To this end, we digested human SEPT6 in pnCS with SpeI/XbaI, ligated the
616 insert to SpeI-digested mouse SEPT2 in pnEA-vH and selected the clones with the
617 correct insert orientation using restriction analysis. Similarly, we digested human
618 SEPT9_i3 in pnCS with SpeI/XbaI, ligated the insert to SpeI-digested human SEPT7ΔN19
619 in pnCS and selected the clones with the correct insert orientation using restriction
620 analysis. The combination of these vectors was used to produce and purify recombinant
621 mammalian SEPT9_i3-containing octamers bearing TEV-cleavable His$_6$-, N-terminally-
622 tagged mouse SEPT2, human SEPT6, human SEPT7ΔN19 and noncleavable Strep-tag-
623 II-, C-terminally-tagged human SEPT9_i3 (Fig. 2 B; left panel in Fig. 3 E).
624 To introduce a TEV cleavage site for Strep-tagged SEPT9_i3 and also generate
625 SEPT9_i1 and SEPT9_i5-containing octamers, and to introduce the missing N-terminal
626 19 residues in SEPT7 (Fig. S1 B), SEPT7ΔN19 being initially erroneously annotated as
627 full-length (Macara et al., 2002), we proceeded as follows. To generate full-length human
628 SEPT7 (UNIPROTKB identifier Q1681-1), we linearized the pnCS plasmid with NdeI/NheI
629 and employed seamless cloning (In-Fusion HD Cloning Plus Kit from Takara Bio, Cat. #
630 638910) with the following primers: forward 5'-
631 AAGGAGATATACATATGTCGGTCAGTGCGAGATCCGCTGCTGCTGAGGAGAGGAG
632 CGTCAACAGCAGCACCATGGTAGCTCAACAGAAGAACCTTG-3' and reverse 5'-
633 GCAGCCTAGGGCTAGCTCTAGACTATTAGGATCcTTAAAAGATCTTCCCTTTCTTCT
634 TGTTCTTTTCC-3'. To insert human SEPT9_i1, SEPT9_i3, and SEPT9_i5 with a TEV-
635 cleavable C-terminal Strep-tag-II upstream of SEPT7, we linearized the SEPT7-
636 containing plasmid with SpeI and used seamless cloning with the following primers:
637 forward 5'-
638 ACAATTCCCCACTAGTAATAATTTTGTTTAACTTTAAGAAGGAGATATACATATGAAG
639 AAGTCT-3' for SEPT9_i1, forward 5'-
640 ACAATTCCCCACTAGTAATAATTTTGTTTAACTTTAAGAAGGAGATATACAtATGGAG
641 AGG-3' for SEPT9_i3 and forward 5'-
642 ACAATTCCCCACTAGTAATAATTTTGTTTAACTTTAAGAAGGAGATATACATATGGC
643 CGACACCCCCAG-3' for SEPT9_i5 and reverse 5'-
644 CAAAATTATTACTAGTTTATTTTTTCGAACTGCGGGTGGCTCCAGCCGCTGCCGCTG

16

645 CCCTGGAAGTAAAGGTTTTCCATCTCTGGGGCTTCTGGC-3' thus generating
646 bicistronic pnCS vectors for co-expression of full-length human SEPT7 and human
647 SEPT9_i (Fig. S1 A, B).

648 Mouse and human SEPT2 differ in 5 residues (I67V, S207N, S352G, S354G, Q359H, the
649 latter residue being human), presenting 98.61% identity. To replace mouse SEPT2 with
650 human SEPT2 in the bicistronic pnEA-vH vector for co-expression of TEV-cleavable His_6-
651 , N-terminally-tagged mouse SEPT2 and human SEPT6 (Fig. S1 A, B), we linearized
652 pnEA-vH with KpnI/NheI and employed seamless cloning with the following primers:
653 forward 5'-
654 ATCATCACAGCAGCGGTACCGGCAGCGGCGAAAACCTTTACTTCCAGGGCCATAT
655 GTCTAAGCAACAACCAACTCAGTTTATAAATC-3' and reverse 5'-
656 ATCTCCTAGGGCTAGCTCTAGACTATTAGGATCCTCACACATGGTGGCCGAGAG-3'.
657 The human SEPT2 cDNA containing several restriction sites routinely used in cloning
658 (KpnI, NheI, BamHI) and to facilitate subsequent subcloning using these sites, we chose
659 to generate a synthetic human SEPT2 coding sequence (Eurofins Genomics, Germany)
660 that employs the codon usage of mouse SEPT2 (which does not contain the mentioned
661 restriction sites) except for the five codons that differ between the two species, for which
662 we used codons encoding the human residues V67, N207, G352, G354, H359.

663 To produce fluorescent octamers, we swapped SEPT2 in the dual expression vector for
664 SEPT2 with its C-terminus tagged with monomeric (V206K) superfolder GFP (msfGFP)
665 (no linker sequence). We generated a synthetic msfGFP coding sequence (Eurofins
666 Genomics, Germany), linearized the dual expression pnEA-vH plasmid with KpnI/NheI
667 and employed two-insert seamless cloning with the following primers: forward 5'-
668 ATCATCACAGCAGCGGTACCGGCAGCGGCGAAAACCTTTACTTCCAGGGCCATAT
669 GTCTAAGCAACAACCAACTCAGTTTATAAATC-3' and reverse 5'-
670 TTGGACACCACATGGTGGCCGAGAGC-3' for SEPT2, and forward 5'-
671 CCATGTGGTGTCCAAGGGCGAGGAGC-3' and reverse 5'-
672 ATCTCCTAGGGCTAGCTCTAGACTATTAGGATCCTTACTTGTACAGCTCATCCATGC
673 CCAG-3' for msfGFP.

674 To generate recombinant human hexamers bearing TEV-cleavable His_6-, N-terminally-
675 tagged human SEPT2, human SEPT6 and TEV-cleavable Strep-tag-II-, C-terminally-
676 tagged human SEPT7 (Fig. S1 A, B; Fig. S2 A, C; Fig. S3 A) we employed a similar
677 cloning strategy. To insert human SEPT2 or human SEPT2-msfGFP in the pnEA-vH
678 vector, we linearized pnEA-vH with KpnI/NheI and employed seamless cloning with the
679 same primers used above in the context of the dual vector. To generate TEV-cleavable
680 Strep-tag-II-, C-terminally-tagged full-length human SEPT7, we linearized the pnCS
681 plasmid with NdeI/NheI and employed seamless cloning with the following primers:
682 forward 5'-
683 AAGGAGATATACATATGTCGGTCAGTGCGAGATCCGCTGCTGCTGAGGAGAGGAG
684 CGTCAACAGCAGCACCATGGTAGCTCAACAGAAGAACCTTG-3' and reverse 5'-
685 GCAGCCTAGGGCTAGCTCTAGACTATTAGGATCCTTATTTTTCGAACTGCGGGTGG

17

686 CTCCAGCCGCTGCCGCTGCCCTGGAAGTAAAGGTTTTCAAAGATCTTCCCTTTCTT
687 CTTGTTCTTTTCC-3'. To insert human SEPT6 upstream of SEPT7, we linearized the
688 SEPT7-containing plasmid with SpeI and used seamless cloning with the following
689 primers: forward 5'-
690 ACAATTCCCCACTAGTAATAATTTTGTTTAACTTTAAGAAGGAGATATACATATGGC
691 AGCGACCGATATAGC-3' and reverse 5'-
692 CAAAATTATTACTAGTCTATTAGGATCCTTAATTTTTCTTCTCTTTGTCTCTCTTCAGA
693 GTCTGTGAG-3' thus generating a bicistronic pnCS vectors for co-expression of human
694 SEPT6 and full-length human SEPT7.
695 Recombinant *Drosophila* hexamers bearing TEV-cleavable His$_6$-, N-terminally-tagged
696 DSep1, untagged or mEGFP-, N-terminally-tagged DSep2 and noncleavable Strep-tag-
697 II-, C-terminally-tagged Peanut were described previously (Fig. S2 B) (Mavrakis et al.,
698 2014; Mavrakis et al., 2016). To generate *Drosophila* hexamers along the lines of the
699 human ones, i.e. with a TEV-cleavable Strep-tag for Peanut and with the C-terminus of
700 DSep1 (the human SEPT2 homolog) tagged with msfGFP (Fig. S2 B; Fig. S3 B), we
701 proceeded as follows. To insert DSep1-msfGFP in the pnEA-vH vector, we linearized
702 pnEA-vH with NdeI/BamHI and employed two-insert seamless cloning with the following
703 primers: forward 5'- ACTTCCAGGGCCATATGGCCGATACAAAGGGCTTTTC-3' and
704 reverse 5'- TTGGACACCTGCTGGGCCTGCATGC-3' for DSep1, and forward 5'-
705 CCAGCAGGTGTCCAAGGGCGAGGAGC-3' and reverse 5'-
706 TAGACTATTAGGATCCTTACTTGTACAGCTCATCCATGCCCAG-3' for msfGFP. To
707 introduce the TEV cleavage site for Peanut in the bicistronic pnCS vector for co-
708 expression with DSep2, we linearized the dual expression pnCS plasmid with NcoI/NheI
709 and employed seamless cloning with the following primers: forward 5'-
710 CGCCAGAAGCCCATGGAG-3' and reverse 5'-
711 GCAGCCTAGGGCTAGCTCTAGACTATTAGGATCCTTATTTTTCGAACTGCGGGTGG
712 CTCCAGCCGCTGCCGCTGCCCTGGAAGTAAAGGTTTTCGAACAGACCCTTCTTTTT
713 CTTCTCCTTCTTGC-3'.
714 All primers for seamless cloning were Cloning Oligo (<60 bp) or EXTREmer (>60 bp)
715 synthesis and purification quality from Eurofins Genomics, Germany. All restriction
716 enzymes were FastDigest enzymes from Thermo Scientific. All plasmids were verified by
717 sequencing (Eurofins Genomics, Germany) after each cloning step, including the
718 midipreps used for protein production.
719
Production and purification of recombinant human and *Drosophila* septin
complexes
722 pnEA-vH and pnCS plasmids were co-transformed into *E. coli* BL21(DE3), and co-
723 transformants selected on LB agar plates with carbenicillin and spectinomycin each at
724 100µg/mL. A single colony was selected to prepare an overnight preculture at 37ºC with
725 LB medium containing antibiotics at 100µg/mL; the volume of the preculture was 1/50 of
726 the final culture volume. Terrific broth with antibiotics at 50µg/mL was inoculated with the

18

727 pre-culture and incubated at 37ºC. We typically prepared 3.5-5 L of culture: the culture
728 volume per Erlenmeyer flask was 1/3 of the flask volume to allow for efficient oxygenation.
729 For nonfluorescent septins we let bacteria grow to $A_{600nm} \sim 2$ before inducing expression
730 with 0.5 mM IPTG for 3 h at 37ºC. For fluorescent septins we let bacteria grow to A_{600nm}
731 $\sim 0.6\text{-}0.8$ before inducing expression with 0.5 mM IPTG for overnight expression at 17ºC;
732 the incubator was protected from light with aluminum foil in this case. The culture was
733 stopped by centrifuging at 3,400 g for 15 min and 4ºC, and the supernatant used to pool
734 all bacteria pellets in 50-mL Falcon tubes, which were further centrifuged at 5,000 g for
735 10 min and 4ºC. Bacteria pellets were stored at -20ºC until protein purification. Bacteria
736 expressing GFP-tagged septins yield yellow-greenish pellets.
737 On the day of purification we resuspended the pellet in ice-cold lysis buffer (50 mM Tris-
738 HCl pH 8, 300 mM KCl, 5 mM $MgCl_2$, 0.25 mg/mL lysozyme, 1 mM PMSF, cOmplete™
739 protease inhibitor cocktail (1 tablet per 50 mL), 10 mg/L DNase I, 20 mM $MgSO_4$) using
740 gentle agitation for 30 min at 4ºC, and lysed cells on ice using a tip sonicator with 5 cycles
741 of 30 s "ON", 15 s "OFF". We typically use 100 mL of lysis buffer for a starting 3.5-5 L
742 culture. The lysate was clarified by centrifugation for 30 min at 20,000 g and 4ºC, the
743 supernatant loaded on a StrepTrap HP column equilibrated with 50 mM Tris-HCl pH 8,
744 300 mM KCl, 5 mM $MgCl_2$ and the column washed with the same buffer. Strep-tag-II-
745 containing septin complexes were eluted with 50 mM Tris-HCl pH 8, 300 mM KCl, 5 mM
746 $MgCl_2$, and 2.5 mM desthiobiotin: desthiobiotin was prepared fresh right before use. All
747 fractions contained in the elution peak were collected. The pooled fractions were then
748 loaded to a HisTrap HP column equilibrated with 50 mM Tris-HCl pH 8, 300 mM KCl, 5
749 mM $MgCl_2$, the column washed with the same buffer, and His_6-tag-containing complexes
750 eluted with 50 mM Tris-HCl at pH 8, 300 mM KCl, 5 mM $MgCl_2$, and 250 mM imidazole.
751 We typically do not concentrate the protein further, thus we collect only the highest-
752 concentration peak fractions ($\sim$0.6 - 1.2 mL). Both affinity column steps were performed
753 on an ÄKTA pure protein purification system (Cytiva). To remove imidazole we either
754 performed an overnight dialysis step or used a PD-10 column, also including DTT in this
755 last step. The final elution buffer, in which septins are stored, was 50 mM Tris-HCl pH 8,
756 300 mM KCl, 5 mM $MgCl_2$, and 1 mM DTT. All purification steps were performed at 4ºC.
757 We typically purify septin complexes in a single day (starting from cell lysis) to minimize
758 unnecessary exposure to proteases and contaminants and maintain protein integrity and
759 functionality.
760 Protein concentrations were assessed with absorbance measurements at 280 nm using
761 the calculated extinction coefficients for the respective complexes, and 20- or 50-µL
762 aliquots were flash-frozen in liquid nitrogen and stored at -80ºC until further use. This
763 protocol yielded typically 0.5-1 mL of purified octamers at $\sim$1-3 mg/mL ($\sim$2-6 µM) and 0.5-
764 1 mL of purified hexamers at $\sim$1-3 mg/mL ($\sim$3-9 µM) from a starting 3.5 L of bacterial
765 culture. Extinction coefficients and molecular masses used for concentration conversions
766 were computed from the primary amino acid sequences using ExPASy
767 (http://web.expasy.org/protparam/) and considering two copies of each full-length septin,

768 tags included, and are summarized in the following table. The calculation of these
769 parameters for mammalian and *Drosophila* hexamers were described in (Mavrakis et al.,
770 2016).

771

	MW (kDa)	ε_{280nm} $L.g^{-1}.cm^{-1}$	
human hexamers	291.8	0.563	1 g/L= 3.4 μM
human octamers-9_i1	422.5	0.505	1 g/L= 2.4 μM
human octamers-9_i3	419.0	0.502	1 g/L= 2.4 μM
human octamers-9_i5	368.7	0.570	1 g/L= 2.7 μM
SEPT2-msfGFP human hexamers	345.2	0.586	1 g/L= 2.9 μM
SEPT2-msfGFP human octamers-9_i1	475.9	0.527	1 g/L= 2.1 μM
SEPT2-msfGFP human octamers-9_i3	472.4	0.525	1 g/L= 2.1 μM
SEPT2-msfGFP human octamers-9_i5	422.1	0.588	1 g/L= 2.4 μM

772

773 Septin preps were used closest to their purification and typically within 2-3 months upon
774 storage at -80ºC. Septin complexes were typically used within 3-4 days upon thawing and
775 not frozen back. Electron microscopy of the purified septin complexes did not show
776 significant aggregation necessitating a gel filtration step, thus size exclusion
777 chromatography used previously (Mavrakis et al., 2014; Mavrakis et al., 2016) was not
778 included. Purified protein was examined as such for EM, whereas it was systematically
779 airfuged right before use for reconstitution assays using fluorescence microscopy to pellet
780 any remaining or formed aggregates upon freezing (see respective methods below). This
781 purification protocol was validated and is routinely used in three different labs (I. Fresnel,
782 I. Curie, TU Delft) with slight variations that do not affect the final result. For example, the
783 order of StrepTrap HP and HisTrap HP columns is inverted, or the nickel-affinity step uses
784 batch resin instead of prepacked columns. This production and purification protocol was
785 used to purify at least six preps of human septin octamers-9_i1, six preps of human septin
786 octamers-9_i3, one prep of human septin octamers-9_i5, and six preps of human septin
787 hexamers. The purification of mammalian septin octamers-9_i3, containing mouse
788 SEPT2, human SEPT6, human SEPT7ΔN19, and human SEPT9_i3 (Fig. 2 B and left
789 panel in Fig. 3 E) was done as described previously (Mavrakis et al., 2014; Mavrakis et
790 al., 2016): the main difference with respect to the protocol described above is that the
791 columns were inverted, nickel affinity used as a first step, and that we employed an
792 additional gel filtration step.

793

794 **Materials and reagents for septin complex production and purification**
795 The sources and identifiers for the chemicals used for recombinant protein production
796 and purification are as follows. *E. coli* BL21(DE3) competent cells from Agilent (200131)
797 or Thermo Scientific (EC0114). Carbenicillin (for pnEA-vH selection) from SIGMA

798   (C3416), Condalab (6803), or Fisher Scientific (Fisher Bioreagents BP2648-1).
799   Spectinomycin (for pnCS selection) from Sigma (S4014) or Fisher Scientific (Fisher
800   Bioreagents BP2957-1). LB broth medium from Sigma (L3022) or Condalab (1231). LB
801   agar from Sigma (L2897) or Condalab (1083). SOC medium from Sigma (S1797) or
802   Fisher Scientific (Fisher Bioreagents BP9740). Terrific Broth from MP Biomedicals
803   (091012017) or Fisher Scientific (Fisher Bioreagents BP2468-10). IPTG from Euromedex
804   (EU0008-C). Imidazole with low absorbance at 280 nm from Fisher Scientific (Fisher
805   Chemical I/0010/53). PMSF from Sigma (78830). Lysozyme from Euromedex (5933).
806   cOmplete™ Protease Inhibitor Cocktail Tablets from Sigma (Roche, 11836145001).
807   DNase I from Sigma (Roche, 10104159001). d-Desthiobiotin from Sigma (D1411). DTT
808   from Sigma (D0632). HisTrap HP 1 mL columns from Cytiva (17524701). StrepTrap HP
809   1 mL columns from Cytiva (28907546). 20K MWCO Slide-A-Lyzer cassettes from Thermo
810   Scientific (87735). PD-10 desalting columns from Cytiva (17085101).
811
812   **SDS-PAGE and Western blot**
813   We assessed septin prep purity and protein integrity by SDS-PAGE and Western blot.
814   Purified septin complexes were analyzed by SDS-PAGE using 4-20% precast
815   polyacrylamide gels (Mini-PROTEAN TGX Gels from Bio-Rad, 4561095), or hand-casted
816   12% or 15% Tris-glycine polyacrylamide gels, followed by staining with InstantBlue
817   Coomassie-stain (Expedeon, ISB1L) (Fig. S1 C-E). Molecular weight markers were
818   Precision Plus Protein All Blue Standards from Bio-Rad (1610373) in all gels shown apart
819   from Fig. S1 C (Pierce Unstained Protein MW Marker from Thermo Scientific, 26610) and
820   Fig. S1 D (PageRuler Plus Prestained Protein Ladder from Thermo Scientific, 26619).
821   SDS-PAGE was performed for each septin prep.
822   Western blots were performed for 2 different preps for each nonfluorescent and SEPT2-
823   msfGFP hexamer and 2 different preps for each nonfluorescent and SEPT2-msfGFP long
824   SEPT9 isoform-containing octamer, with similar results. Gels for Western blot detection
825   were loaded with 10 ng of purified protein. Gel, transfer membrane (Immobilon-P^{SQ}
826   membrane, Sigma ISEQ85R), filter pads and filter papers were incubated in transfer
827   buffer (25 mM Tris, 192 mM glycine, 20% methanol) for 15 minutes before assembly in
828   the Mini Trans-Blot transfer cell (Bio-Rad, 1703935). The transfer was done for 16 h at
829   4ºC and at 110 mA constant current. The membrane was then blocked in a 5% w/v dry
830   nonfat milk TBS-T solution (20 mM Tris-HCl pH 7.5, 200 mM NaCl, 0.1 % v/v Tween20)
831   for 2 h under constant agitation. Primary and secondary antibodies were diluted in the
832   same blocking solution and incubated over the membrane for 60 min each under constant
833   agitation. Between antibody incubations, membranes were washed 3 times for 10 min
834   with TBS-T, the very last wash before detection only with TBS. To detect specific septins
835   in recombinant human hexamers and octamers, we used rabbit anti-SEPT2 (1:2,500,
836   Sigma, HPA018481), rabbit anti-SEPT6 (1:1,500, Santa Cruz Biotechnology, sc-20180),
837   rabbit anti-SEPT7 (1:200, Santa Cruz Biotechnology, sc-20620), rabbit anti-SEPT9
838   (1:1,500, Proteintech, 10769-1-AP), and HRP-conjugated anti-rabbit antibody (1:10,000,

21

839   Cytiva, NA934). Chemiluminescent detection was done with an Amersham ImageQuant
840   800 imager (Cytiva, 29399481) using Amersham ECL Select Western Blotting Detection
841   Reagent (Cytiva, RPN2235) diluted 5 times in Milli-Q water. The membrane was
842   incubated with the diluted reagent for 30 s, and washed for 10 s in TBS right before image
843   acquisition. Images were collected in time series mode every 10 s, for a total of 50 images,
844   and processed with ImageQuantTL software for molecular size calculation. In 4-20% Tris-
845   glycine gels, the apparent mass of SEPT6 was larger than its calculated one by ~3 kDa,
846   resulting in a band right above the one of SEPT7 that migrated as expected. The TEV-
847   Strep-tag-II of SEPT7 in hexamer preps adds 2.2 kDa to the SEPT7 band which thus
848   migrates much closer to SEPT6, making SEPT6 and SEPT7 bands hard to make out. All
849   SEPT9 isoforms migrated much more slowly than their calculated masses: the apparent
850   masses of the two long isoforms were larger by ~ 12-13 kDa, the one of the short isoform
851   by ~ 5 kDa. Western blot analysis of hexamer and octamer preps showed that all septins
852   were intact, with the long N-terminal extension of SEPT9 being the most sensitive to
853   proteolysis (Fig. S1 F). The purity and protein integrity of septins in preps, as well as the
854   identification of protein bands in gels were corroborated by mass spectrometry analysis
855   (see respective section below).
856
857   **Mass spectrometry analysis and data processing**
858   For analysis of septin hexamers and octamers (one prep for each hexamer and for each
859   long SEPT9 isoform-containing octamer), 1 µg of sample was loaded on 4–12% NuPAGE
860   Novex Bis-Tris polyacrylamide gels (Thermo Scientific, NP0322BOX) and ran for 7 min
861   at 80V to stack proteins in a single band. The gel was further stained with Imperial Protein
862   Stain (Thermo Scientific, 24615), destained in water and proteins cut from the gel. Gel
863   pieces (protein stack or cut protein bands) were subjected to in-gel trypsin digestion after
864   cysteine reduction and alkylation (Shevchenko et al., 2006). Peptides were extracted from
865   the gel and dried under vacuum. Samples were reconstituted with 0.1% trifluoroacetic
866   acid in 2% acetonitrile and analyzed by liquid chromatography (LC)-tandem MS (MS/MS)
867   using a Q Exactive Plus Hybrid Quadrupole-Orbitrap (Thermo Scientific,
868   IQLAAEGAAPFALGMBDK) online with a nanoLC UltiMate 3000 chromatography system
869   (Thermo Scientific, ULTIM3000RSLCNANO). 2 microliters corresponding to 10 % of
870   digested protein were injected in duplicate on the system. After pre-concentration and
871   washing of the sample on a Acclaim PepMap 100 C18 column (2 cm × 100 µm i.d., 100
872   Å pore size, 5 µm particle size, Thermo Scientific 164564-CMD), peptides were separated
873   on a LC EASY-Spray C18 column (50 cm × 75 µm i.d., 100 Å pore size, 2 µm particle
874   size, Thermo Scientific ES803) at a flow rate of 300 nL/min with a two-step linear gradient
875   (2-20% acetonitrile in 0.1 % formic acid for 40 min and 20-40% acetonitrile in 0.1 % formic
876   acid for 10 min). For peptide ionization in the EASY-Spray source, spray voltage was set
877   at 1.9 kV and the capillary temperature at 250°C. All samples were measured in a data-
878   dependent acquisition mode. Each run was preceded by a blank MS run in order to
879   monitor system background. The peptide masses were measured in a survey full scan

22

880 (scan range 375-1500 m/z, with 70 K FWHM resolution at m/z=400, target AGC value of
881 $3.00×10^6$ and maximum injection time of 100 ms). Following the high-resolution full scan
882 in the Orbitrap, the 10 most intense data-dependent precursor ions were successively
883 fragmented in the HCD cell and measured in Orbitrap (normalized collision energy of 27
884 %, activation time of 10 ms, target AGC value of $1.00×10^5$, intensity threshold $1.00×10^4$
885 maximum injection time 100 ms, isolation window 2 m/z, 17.5 K FWHM resolution, scan
886 range 200 to 2000 m/z). Dynamic exclusion was implemented with a repeat count of 1
887 and exclusion duration of 10 s.
888 Raw files generated from mass spectrometry analysis were processed with Proteome
889 Discoverer 1.4.1.14 (Thermo Scientific) to search against the proteome reference of the
890 *Escherichia coli* protein database (4,391 entries, extracted from Uniprot in August 2020).
891 The original fasta file was populated with the sequences of the septin constructs
892 contained in the measured preps. Database search with Sequest HT was done using the
893 following settings: a maximum of two missed trypsin cleavages allowed, methionine
894 oxidation as a variable modification and cysteine carbamidomethylation as a fixed
895 modification. A peptide mass tolerance of 10 ppm and a fragment mass tolerance of 0.6
896 Da were allowed for search analysis. Only peptides with high Sequest scores were
897 selected for protein identification. False discovery rate was set to 1% for protein
898 identification.
899 To measure the relative protein abundance in septin preps we employed the Top3
900 quantitation approach based on the correlation between the sum of the three most intense
901 peptide ions of a given protein and its absolute abundance (Silva et al.,
902 2006). We divided the Top3 value of each identified protein in the protein stack by the
903 sum of all Top3 values, generating a relative Top3 abundance measure, which
904 correlates with the mol fraction of the protein. Septins constituted >97% of the total protein
905 content, with the remaining <3% including GTP cyclohydrolase, biotin carboxylase and
906 several chaperones (DnaK, DnaJ, GrpE, 60 kDa chaperonin). The results for molar
907 fractions down to 0.02% are shown in Fig. S1 G for a hexamer and two octamer preps.
908 The obtained mol fractions of septins, compared with the expected ones for hexamers
909 (33%) and octamers (25%), point to the isolation of stoichiometric hexamers and
910 octamers.
911 Tryptic peptides were used to identify and assign each septin to the detected bands by
912 Coomassie staining, both for nonfluorescent and SEPT2-msfGFP hexamers and
913 octamers, as shown in Fig. 1 D and Fig. S1 C-E, and septin band assignment was in line
914 with the Western blot analysis (Fig. S1 F). Examples of tryptic peptide coverage for
915 individual septins in recombinant hexamer, octamer-9_i1 and octamer-9_i3 preps are
916 shown in Fig. S1 H, with coverages of 82% (SEPT2), 74% (SEPT6) and 70% (SEPT7)
917 for hexamers, 82% (SEPT2), 70% (SEPT6), 69% (SEPT7) and 80% (SEPT9_i1) for
918 octamers-9_i1, and 82% (SEPT2), 85% (SEPT6), 68% (SEPT7) and 84% (SEPT9_i3) for
919 octamers-9_i3. Tryptic peptides were identified throughout the sequence of each septin,
920 including coiled-coils of all septins and the common N-terminal extension of the long

921 SEPT9 isoforms, which together with the apparent band sizes from SDS-PAGE and the
922 Western blot analysis (Fig. 1D; Fig. S1 F) supports that the isolated septin complexes are
923 intact. Coomassie-stained bands other than the annotated ones in our figures were
924 identified as degradation products of septins or/and contaminants already identified in the
925 analysis of the complexes from protein stacks. Degradation band analysis from different
926 preps suggested that the coiled-coils of SEPT2 and SEPT7 and the N-terminal extension
927 of SEPT9 are most sensitive to proteolysis; the sensitivity of the latter to proteolysis was
928 in line with Western blots using antibodies against the C-terminal half of SEPT9 (Fig. S1
929 F).
930

Native PAGE

932 Native PAGE was performed on 4-16% NativePAGE Novex Bis-Tris polyacrylamide gels
933 (Thermo Scientific, BN1002BOX) following instructions from the manufacturer. Briefly,
934 two µg of recombinant septin complexes, in their elution buffer (50 mM Tris-HCl pH 8,
935 300 mM KCl, 5 mM $MgCl_2$, 1 mM DTT), were diluted with water and 4x native PAGE
936 sample buffer (Thermo Scientific, BN2003) to achieve a total KCl/NaCl concentration of
937 ~100 mM and 1x native sample buffer, and were loaded in each gel well. Electrophoresis
938 was performed at 150 V constant voltage until the migration front had reached one third
939 of the gel, when dark cathode buffer was replaced with light anode buffer, then
940 electrophoresis was pursued at 150 V until the migration front had reached the bottom of
941 the gel. Gels were destained in 25% methanol and 10% acetic acid to eliminate most of
942 the background (Coomassie stain from running buffer), then washed twice in pure water
943 for 30 min, placed in Imperial Protein Stain (Thermo Scientific, 24615) for one hour and
944 destained in pure water overnight. Molecular weight standards were NativeMark
945 Unstained Protein Standard (Thermo Scientific, LC0725). Native PAGE was performed
946 for 2 independent preps for human hexamers and for each long SEPT9 isoform-
947 containing octamer, with similar results.
948 Hexamers migrated with an apparent size of ~310 kDa, in line with the calculated one
949 (292 kDa). Octamers for both long SEPT9 isoform-containing octamers migrated with
950 apparent sizes of ~600 kDa, thus much more slowly than their theoretical sizes (423 kDa
951 and 419 kDa, respectively), in line with reported gel filtration and density gradient
952 centrifugation experiments showing that the long SEPT9 isoform-specific N-terminal
953 extension confers a significant increase in the hydrodynamic radius slowing down
954 octamer migration in native PAGE (Sellin et al., 2014).
955

Modeling of human septin octamers

957 Models of human septin octamers were generated in order to analyze and interpret the
958 analytical ultracentrifugation sedimentation velocity experiments. A series of structures of
959 the GTP-binding domains (GBDs) of SEPT2, 6, 7 and 9 have been solved by X-ray
960 crystallography (Rosa et al., 2020; Valadares et al., 2017), with some flexible loops
961 partially missing. The homology modelling software, SWISS-MODEL (Waterhouse et al.,

24

2018), was used to complete the existing GBD structures. To search for templates, SWISS-MODEL uses BLAST (Camacho et al., 2009) and HHblits (Steinegger et al., 2019) for related evolutionary structures matching the target sequence within the SWISS-MODEL Template Library (SMTL version 2020-12-09, last included PDB release: 2020-12-04). For each identified template, the quality of the resulting model is predicted from features of the target-template alignment, and the template with the highest quality is selected for model building using ProMod3. Coordinates which are conserved between the target and the template are copied from the template to the model. Insertions and deletions are remodelled using a fragment library. Finally, the geometry of the resulting model is regularized by using a CHARMM22/CMAP protein force field (Mackerell et al., 2004). The global and per-residue model quality is assessed using the QMEAN scoring function (Studer et al., 2020). Due to the lack of structural information for the long SEPT9 isoform N-terminal extension, the absence of structural homologs for this region (using Phyre2 and SWISS-MODEL) and secondary structure predictions of disorder for this region (using Quick2D), this region was not modeled. Similarly, the lack of structural information for the short N-terminal extensions of SEPT2, 6, and 7, including the $\alpha0$ helices, prompted us not to model these regions. GBD models, starting right after the end of the $\alpha0$ helices and until the end of the $\alpha6$ helices, were generated for SEPT2 37-306 (template PDB 6UPA), SEPT6 40-308 (template PDB 6UPR), SEPT7 48-316 (template PDB 6N0B), and SEPT9 295-568 (template PDB 5CY0; numbering based on SEPT9_i1). To account for the contribution of the predicted coiled-coils in the C-terminal extensions of SEPT2, 6 and 7 to the hydrodynamic properties of the complexes and thus their sedimentation behavior, we extended the GBD models to include the C-terminal domain from the end of the $\alpha6$ helix onwards. Delineation of coiled-coil features was based on secondary structure prediction via Quick2D (Zimmermann et al., 2018). This tool integrates secondary structure predictions from different softwares, including coiled-coil prediction via MARCOIL (Delorenzi and Speed, 2002), PCOILS (Gruber et al., 2006) and COILS (Lupas et al., 1991). The consensus sequences assigned by all three coiled-coil prediction algorithms were used for modeling coiled-coil helices with CCFold software (Guzenko and Strelkov, 2018). The resulting coiled-coils encompass residues 310-349, 321-406, and 336-421 for SEPT2, 6, and 7, respectively.

The models built with SWISS-MODEL and CCFold were still missing the connections between the GBDs and coiled-coils for SEPT2, 6, and 7, the ends of the C-terminal domains right after the predicted CCs, and the C-terminal domain of SEPT9 after the $\alpha6$ helix. Phyre2 (Kelley et al., 2015) was used to construct these flexible parts *ab initio* for SEPT2, 7 and 9*;* and by homology for the very end of SEPT6 as a structural homolog was found by the software. The different models were generated in the context of the full proteins for higher accuracy. The flexible parts linking the GBDs and coiled-coils and the remaining C-terminal features were isolated from the resulting models with PyMOL (open-source software). GBDs, coiled-coils and flexible parts were then combined with PyMOL. The connections between the GBDs and the coiled-coils for SEPT6 and 7 being of

25

1003   different length and to allow for the aligning of coiled-coil helices of SEPT6 and 7, these
1004   connections were stretched out so that they cover the same distance between the GBDs
1005   and the start of the coiled-coils without any steric clashes. In the case of SEPT2, the 3
1006   residues between the GBD and the coiled-coil were built directly with PyMOL.
1007   Tetrameric SEPT2-SEPT6-SEPT7-SEPT9 and octameric SEPT2-SEPT6-SEPT7-
1008   SEPT9-SEPT9-SEPT7-SEPT6-SEPT2 complexes were built by fitting the modeled
1009   structures to the crystal structure of the SEPT2-SEPT6-SEPT7 trimer (PDB 2QAG)
1010   (Sirajuddin et al., 2007). The PDB files of the modeled tetramers and octamers, with or
1011   without the C-terminal extensions, were then used in HullRad to determine their diffusion
1012   coefficient and estimate their sedimentation coefficient (see section on analytical
1013   ultracentrifugation below). Given that the long SEPT9 isoform N-terminal extensions are
1014   not contained in the model structures, the calculated diffusion coefficients were the same
1015   for all three SEPT9 isoforms (Fig. 1G and Fig. S1 I).
1016
1017   **Analytical ultracentrifugation**
1018   A sedimentation velocity experiment was carried out for one prep each of octamers-9_i1
1019   (0.75 mg/mL) and octamers-9_i3 (0.5 mg/mL), at 40,000 rpm and 20°C in a Beckman
1020   Optima XL-A analytical ultracentrifuge, using 12 mm double sector centerpieces in an
1021   AN-50 Ti rotor (Beckman Coulter). Scans were acquired in continuous mode at 280 nm,
1022   in the absorbance range of 0.1 to 1. The partial specific volume of the proteins and the
1023   density and viscosity of the buffer were calculated with SEDNTERP (Laue et al., 1992).
1024   At 20°C, the calculated partial specific volume for octamers-9_i1 and -9_i3 was 0.735
1025   mL.g^{-1}. The density and viscosity of the buffer (50 mM Tris-HCl pH 8, 300 mM KCl, 5 mM
1026   MgCl$_2$, 1 mM DTT) were 1.014 g.mL^{-1} and 0.0102 poise, respectively. The data recorded
1027   from moving boundaries were analyzed in terms of continuous size distribution functions
1028   of sedimentation coefficient, $c(s)$, using the program SEDFIT (Schuck and Rossmanith,
1029   2000) and the apparent sedimentation coefficient at 20°C in water ($S_{20,W}$) determined by
1030   peak integration.
1031   A short column sedimentation equilibrium experiment was carried out for one prep each
1032   of SEPT2-msfGFP hexamers and SEPT2-msfGFP octamers-9_i5, at 11,000 rpm in a
1033   Beckman Optima XL-A analytical ultracentrifuge, using 60 μL of protein loading
1034   concentrations from 0.5 to 1.5 mg.mL^{-1}, in a six-channel epon charcoal-filled centerpiece
1035   in an AN-50 Ti rotor (Beckman Coulter). Septins were in 50 mM Tris-HCl pH 8, 300 mM
1036   KCl, 5 mM MgCl$_2$, and 1 mM TCEP. Scans were acquired at appropriate wavelengths
1037   (280 nm and 485 nm) when sedimentation equilibrium was reached at 4°C. Average
1038   molecular masses were determined by fitting a sedimentation equilibrium model for a
1039   single sedimenting solute to individual data sets with SEDPHAT.
1040   To determine the theoretical sedimentation coefficient, the PDB file of a given model
1041   (tetramer, hexamer or octamer, with or without coiled-coils, and with coiled-coils in
1042   different orientations) was analyzed using HullRad (Fleming and Fleming, 2018) to
1043   determine the translational diffusion coefficient, D. The estimated sedimentation

1044 coefficient, *s*, was then obtained using the theoretical molecular mass, *M*, for each
1045 complex and the Svedberg equation below, with v the partial specific volume of the
1046 protein, ρ the solvent density, *R* the gas constant and *T* the temperature:

1047
1048 $$s = \frac{M\,(1\text{-}\overline{v}\rho)D}{RT}$$
1049

1050 The theoretical sedimentation coefficients calculated in this manner are shown in Fig. 1G
1051 and Fig. S1 I. The experimentally measured ones for octamers-9_i1 and -9_i3, and the
1052 comparison with the estimated ones in the absence of coiled-coils or in the absence of
1053 the long SEPT9 isoform N-terminal extension (SEPT9_i5) are consistent with intact
1054 octamers-9_i1 and -9_i3.

1055

1056 **Preparation of flow cells for fluorescence microscopy of *in vitro* reconstituted actin**
1057 **and septins**
1058 Microscope glass slides and coverslips were cleaned for 15 min in base-piranha solution
1059 (Milli-Q water, 30% ammonium hydroxide, 35% hydrogen peroxide at a 5:1:1 volume
1060 ratio), rinsed twice, 5 min each, with Milli-Q water in a bath sonicator, and stored in 0.1 M
1061 KOH up to one month. Right before assembling flow cells, slides and coverslips were
1062 rinsed twice, 5 min each, with Milli-Q water and dried with synthetic air. Flow cells with
1063 ~10 μL channels were assembled by sandwiching ~2-mm-wide and ~2.5-cm-long strips
1064 of Parafilm between a cleaned glass slide and coverslip and melting on a hot plate at
1065 120°C (Fig. 4 B). The resulting chambers were passivated by incubating for 45 min with
1066 1 M KOH, rinsing with actin polymerization buffer (see composition in the respective
1067 section), incubating for another 45 min with 0.2 mg/mL PLL-PEG, and rinsing with actin
1068 polymerization buffer (5 mM Tris-HCl pH 8, 50 mM KCl, 1 mM MgCl$_2$, 0.2 mM Na$_2$ATP, 1
1069 mM DTT). Flow cells were placed in a Petri-dish along with tissue paper soaked in water
1070 to prevent flow channels from drying during the incubation steps and until use.
1071 The sources and identifiers for the materials and chemicals are as follows. Glass slides
1072 (26x76 mm) from Thermo Scientific (AA00000102E01FST20). Glass coverslips (24x60
1073 mm) from Thermo Scientific (BB02400600A113FST0). Ammonium hydroxide solution
1074 from SIGMA (221228). Hydrogen peroxide solution from SIGMA (95299). PLL-PEG from
1075 SuSoS AG (PLL(20)-g[3.5]-PEG(2)).

1076

1077 **Sample preparation for fluorescence microscopy of *in vitro* reconstituted actin and**
1078 **septins**
1079 Lyophilized rabbit skeletal muscle G-actin was resuspended to 5 mg/mL (119 μM) in G-
1080 buffer (5 mM Tris-HCl pH 8, 0.2 mM Na$_2$ATP, 0.1 mM CaCl$_2$, 1 mM DTT), aliquots snap-
1081 frozen in liquid nitrogen and stored at −80°C. Frozen aliquots were thawed and
1082 centrifuged for 30 min at 120,000 g in a benchtop Beckman air-driven ultracentrifuge
1083 (Beckman Coulter Airfuge, 340401) to clear the solution from aggregates. Clarified G-
1084 actin was kept at 4°C and used within 3-4 weeks.

27

1085   For reconstitution experiments, G-actin was diluted with G-buffer to 5 μM, and
1086   polymerized at 1 μM final concentration in actin polymerization buffer (5 mM Tris-HCl pH
1087   8, 50 mM KCl, 1 mM $MgCl_2$, 0.2 mM Na_2ATP, 1 mM DTT), additionally containing 1 mM
1088   Trolox, 2 mM protocatechuic acid (PCA), 0.1 μM protocatechuate 3,4-dioxygenase (PCD)
1089   and 0.1% w/v methylcellulose. Trolox and the enzymatic oxygen scavenging system
1090   PCA-PCD were used to minimize photobleaching during fluorescence imaging (Cordes
1091   et al., 2009; Shi et al., 2010). Methylcellulose was used as a crowding agent to keep actin
1092   filaments close to the surface and facilitate their observation. To fluorescently label actin
1093   filaments, we polymerized G-actin in the presence of 1 μM Alexa Fluor 568-conjugated
1094   phalloidin.
1095   For actin-septin reconstitution experiments, thawed septin aliquots were cleared for 15
1096   min at 120,000 g in a Beckman airfuge right before use. To polymerize G-actin in the
1097   presence of septins, we followed the same procedure as above, but mixed G-actin with
1098   septins, either nonfluorescent ones or GFP-labeled septins (at 20% GFP molar ratio for
1099   octamers-9_i1 and -9_i3, and 100% GFP for octamers-9_i5) to a final septin
1100   concentration of 0.3 μM, right before polymerization. Actin and actin-septin samples were
1101   prepared with a final volume of 10 μL, were loaded immediately into PLL-PEG-passivated
1102   flow channels upon mixing of the components to start polymerization, and flow channels
1103   were sealed with VALAP (1:1:1 vasoline:lanoline:paraffin). The contributions of KCl and
1104 $MgCl_2$ from the septin elution buffer were taken into account to yield the same final
1105   composition of actin polymerization buffer. Actin and actin-septin samples were typically
1106   incubated overnight at room temperature in the dark before observation. Actin-septin
1107   assays were repeated at least four times, using at least two different preps from each
1108   nonfluorescent and fluorescent hexamers, 8-mers-9_i1 and 8-mers-9_i3, and one prep
1109   from fluorescent 8-mers-9_i5, yielding similar results.
1110   To polymerize septins in the absence of actin, we followed the same procedure as above,
1111   but replaced the G-actin solution with G-buffer. Septins were also polymerized in the
1112   absence of actin by overnight dialysis against a low-salt buffer (50 mM Tris-HCl pH 8, 50
1113   mM KCl, 5 mM $MgCl_2$, 1 mM DTT) at 4°C, then loaded into PLL-PEG-passivated flow
1114   channels in the presence of 1 mM Trolox, 2 mM PCA, 0.1 μM PCD and 0.1% w/v
1115   methylcellulose, and sealed as described above for observation. Septins were used at
1116   20% or 100% GFP molar ratio, yielding similar results. Septin polymerization assays were
1117   repeated at least five times, using at least two different preps from each nonfluorescent
1118   and fluorescent hexamers, 8-mers-9_i1 and 8-mers-9_i3, and one prep from fluorescent
1119   8-mers-9_i5, yielding similar results.
1120   Actin-septin samples with mammalian septin hexamers (Fig. S3 C) were prepared as
1121   above with the difference that septins were nonfluorescent, and fluorescent actin was
1122   Alexa Fluor 488-conjugated G-actin (10% molar ratio) as described previously (Mavrakis
1123   et al., 2014; Mavrakis et al., 2016). G-actin polymerization in this case occurred in the
1124   presence of nonfluorescent phalloidin.

1125 The sources and identifiers for proteins, materials and chemicals are as follows. Rabbit
1126 skeletal muscle G-actin from Cytoskeleton, Inc. (AKL99). Alexa Fluor 568-phalloidin from
1127 Thermo Scientific (A12380). Nonfluorescent phalloidin from Sigma (P2141).
1128 Methylcellulose from Sigma (M0512). Trolox from Sigma (238813). Protocatechuic acid
1129 from Sigma (03930590). Protocatechuate 3,4-dioxygenase from Sigma (P8279). 20K
1130 MWCO Slide-A-Lyzer MINI dialysis devices from Thermo Scientific (69590).
1131

Fluorescence microscope image acquisition and processing
1132
1133 Samples were imaged on an optical setup employing a confocal spinning disk unit (CSU-
1134 X1-M1 from Yokogawa) connected to the side-port of a Perfect Focus System-equipped
1135 inverted microscope (Eclipse Ti2-E from Nikon Instruments), using a Nikon Plan Apo
1136 ×100/1.45 NA oil immersion objective lens, 488- and 561-nm Sapphire laser lines
1137 (Coherent) and an iXon Ultra 888 EMCCD camera (1024×1024 pixels, 13×13 μm pixel
1138 size, Andor, Oxford Instruments), resulting in an image pixel size of 65 nm. Images were
1139 acquired with an exposure time of 0.1 s. Time-lapse sequences were acquired with a time
1140 interval of 0.5 s for a duration of 15 s. Actin filaments and actin-septin bundles were
1141 imaged close to the surface. Septin filament bundles were also found at the surface, but
1142 the extensive clusters of interconnected human septin filament bundles were observed
1143 floating in the bulk of the flow channels. To capture such clusters, z-stacks were acquired
1144 over 10-50 μm using a Δz interval of 0.5 μm. The images shown correspond to octamers-
1145 9_i1 polymerized with 20% GFP-septins (Fig. 3 A), octamers-9_i3 polymerized with 100%
1146 GFP-septins (Fig. 3 B), octamers-9_i5 polymerized with 100% GFP-septins (Fig. 3 C),
1147 hexamers polymerized with 100% GFP-septins (Fig. S 2 A), and *Drosophila* hexamers
1148 polymerized with 20% GFP-septins (Fig. S 2 B). All examples shown depict
1149 polymerization upon dilution into low salt apart from Fig. S 2 A (left panel) which shows
1150 polymerization upon dialysis into low salt.
1151 Images were processed with the open-source image processing software ImageJ/Fiji.
1152 Images of actin filaments and actin-septin bundles are from single planes. Images of
1153 septin filament bundles are from maximum-intensity z projections except for *Drosophila*
1154 septins, for which single planes are shown given that their bundles were typically found
1155 primarily at the surface. The contrast of all images shown was adjusted post-acquisition
1156 so that both dim and bright structures are visible. To saturate the signal in the actin
1157 bundles and make the weaker-intensity signal of single/thinner actin filaments visible, the
1158 contrast was enhanced on purpose (images labeled "contrast enhancement" in Fig. 4 C-
1159 E and Fig. S3 A-B). All images shown use an inverted grayscale, with bright signals
1160 appearing black in a white background.
1161 Actin-septin samples with mammalian septin hexamers (Fig. S3 C) were imaged with a
1162 Nikon Apo TIRF ×100/1.49 NA oil immersion objective lens mounted on an Eclipse Ti
1163 microscope (Nikon Instruments) using a 491 nm laser line and imaged with a QuantEM
1164 512SC EMCCD camera (Photometrics). Images were acquired with an exposure time of
1165 0.1 s.

1166

1167 **Transmission electron microscopy**

1168 **Negative stain electron microscopy.** 4 µL of sample at final septin concentrations of
1169 0.01-0.02 mg/mL (~25-50 nM) for high salt conditions (50 mM Tris-HCl pH 8, 300 mM
1170 KCl, 2 mM MgCl$_2$) or 0.05-0.1 mg/mL (~125-250 nM) for low salt conditions (50 mM Tris-
1171 HCl pH 8, 50 mM KCl, 2 mM MgCl$_2$) were adsorbed for 30 s (for high salt conditions) to 1
1172 h in a humid chamber (for low salt conditions) on a glow-discharged carbon-coated grid
1173 (Electron Microscopy Sciences, CF300-CU). For low salt conditions, septins were
1174 polymerized by dilution into low-salt buffer and incubated for 1 h to overnight at room
1175 temperature before grid adsorption. In the case of GFP-labeled septins, septins were
1176 polymerized without mixing with nonfluorescent ones. The grids were rinsed and
1177 negatively stained for 1 min using 1% w/v uranyl formate. Images for the qualitative
1178 examination of the morphology of septin assemblies were collected using a Tecnai Spirit
1179 microscope (Thermo Scientific, FEI) operated at an acceleration voltage of 80kV and
1180 equipped with a Quemesa camera (Olympus). In addition to the EM experiments
1181 described above which were performed at I. Curie, EM was also performed at TU Delft
1182 following a similar protocol. Septins were polymerized by dilution into a low-salt buffer (25
1183 mM Tris-HCl pH 7.4, 50 mM KCl, 2.5 mM MgCl$_2$, 1 mM DTT) at a final septin concentration
1184 of 1 µM for 1 h. The solution was then adsorbed to a glow discharged grid for 1 min,
1185 rinsed, negatively stained with 2% w/v uranyl acetate for 30 s and air dried. Images were
1186 collected with a JEM-1400plus TEM microscope (JEOL) operated at 120kV equipped with
1187 4k X 4k F416 CMOS camera (TVIPS). Septin filament bundle length and width
1188 measurements (Fig. S2 E) were made with the line tool in ImageJ/Fiji, and boxplots
1189 generated in Matlab. Electron microscopy was performed with at least two different preps
1190 from each nonfluorescent and fluorescent hexamers, 8-mers-9_i1 and 8-mers-9_i3. The
1191 images shown correspond to nonfluorescent octamers-9_i1 (Fig. 3 D, i-ii) and octamers-
1192 9_i3 (Fig. 3 E), SEPT2-msfGFP octamers-9_i1 (Fig. 3 D, iii-v), SEPT2-msfGFP hexamers
1193 (Fig. S 2 C), and nonfluorescent mammalian hexamers (Fig. S 2 D).

1194

1195 **Two-dimensional image processing for single-particle EM images.** Images for single-
1196 particle analysis were collected using a Lab6 G2 Tecnai microscope (Thermo Scientific)
1197 operated at an acceleration voltage of 200 kV. Images were acquired with a 4k X 4k F416
1198 CMOS camera (TVIPS) in an automated manner using the EMTools software suite
1199 (TVIPS) with a pixel size of 2.13 Å and an electron dose of about 15 electrons/Å^2. 2D
1200 processing was carried out on septin rods incubated in high salt conditions (50 mM Tris-
1201 HCl pH 8, 300 mM KCl, 2 mM MgCl$_2$) to determine the integrity of the complexes and
1202 pinpoint the arrangement of septin subunits within the complex. About 100 images were
1203 collected for each septin complex for image processing. Individual particles (septin rods)
1204 were hand-picked from the images using the boxer tool from the EMAN software suite
1205 (Ludtke et al., 1999). About 20-30 particles (203x203 pixel boxes) were extracted per
1206 image. Subsequent processing was carried out using SPIDER (Frank et al., 1996). After
1207 normalization of the particles, a non-biased reference-free algorithm was used to

30

1208 generate 20 classes. Those classes were further used as references to pursue 2D
1209 multivariate statistical analysis. Multi-reference alignment followed by hierarchical
1210 classification involving principal component analysis was thereafter carried out to
1211 generate classes containing 50-100 particles. Each of the classes are representative of
1212 specific features within a given sample. This processing enabled us to quantify the
1213 distribution of particles in each dataset regarding the dimension of the rods as well as the
1214 presence of an additional electron density (GFP-tag or antibody). For mammalian
1215 octamers-9_i3 (Fig. 2 B), 4000 particles were selected with a distribution of 50%
1216 octamers, 23.7% heptamers, 23.5 % hexamers, 1.4% pentamers and 1.4% tetramers.
1217 For human SEPT2-msfGFP octamers-9_i1 (Fig. 2 C), 3266 particles were picked with a
1218 distribution of 57.9% octamers, 32.1% heptamers and 10.1% hexamers. An additional
1219 density towards the ends of the rods was pinpointed for 46.2% of the particles. For human
1220 SEPT2-msfGFP hexamers (Fig. 2 D), 2976 particles were selected with a distribution of
1221 97.7% hexamers and 2.3% pentamers. An additional density towards the ends of the rods
1222 could be pinpointed for 53.6% of the particles. For human octamers-9_i1 incubated with
1223 SEPT9 antibodies (Fig. 2 C), 2352 particles were picked with a distribution of 13.7%
1224 octamers, 72.1% heptamers and 14.2% hexamers. 52.6% of the dataset exhibited an
1225 additional density towards the center of the rod that could be related to the presence of
1226 the antibody. Septin octamers were incubated with a rabbit antibody against the very C-
1227 terminus of SEPT9 (Pizarro-Cerda et al., 2002) for 30 min prior to grid adsorption and
1228 staining.

Acknowledgements

1258   The authors declare no competing financial interests.

1259   Author contributions: F. Iv, A. Llewellyn, M. Belhabib, L. Ramond, A. Di Cicco, K.
1260   Nakazawa: investigation; C. Silva Martins, G. Castro-Linares, C. Taveneau, F-C Tsai, P.
1261   Barbier, P. Verdier-Pinard, L. Camoin, S. Audebert, investigation, writing – review &
1262   editing; R. Vincentelli, supervision, resources; J. Wenger, funding acquisition,
1263   supervision, writing – review & editing; S. Cabantous, supervision, writing – review &
1264   editing; G. H. Koenderink, conceptualization, funding acquisition, supervision, writing –
1265   review & editing; A. Bertin, conceptualization, supervision, investigation, writing – review
1266   & editing; M. Mavrakis, conceptualization, methodology, funding acquisition, project
1267   administration, supervision, investigation, writing – original draft, writing – review & editing
1268

References

1270   Akhmetova, K., M. Balasov, R.P. Huijbregts, and I. Chesnokov. 2015. Functional insight
1271   into the role of Orc6 in septin complex filament formation in Drosophila. *Mol Biol*
1272   *Cell*. 26:15-28.
1273   Akil, A., J. Peng, M. Omrane, C. Gondeau, C. Desterke, M. Marin, H. Tronchere, C.
1274   Taveneau, S. Sar, P. Briolotti, S. Benjelloun, A. Benjouad, P. Maurel, V. Thiers, S.
1275   Bressanelli, D. Samuel, C. Brechot, and A. Gassama-Diagne. 2016. Septin 9
1276   induces lipid droplets growth by a phosphatidylinositol-5-phosphate and
1277   microtubule-dependent mechanism hijacked by HCV. *Nat Commun*. 7:12203.
1278   Bai, X., J.R. Bowen, T.K. Knox, K. Zhou, M. Pendziwiat, G. Kuhlenbaumer, C.V. Sindelar,
1279   and E.T. Spiliotis. 2013. Novel septin 9 repeat motifs altered in neuralgic
1280   amyotrophy bind and bundle microtubules. *The Journal of cell biology*. 203:895-
1281   905.
1282   Bertin, A., M.A. McMurray, P. Grob, S.S. Park, G. Garcia, 3rd, I. Patanwala, H.L. Ng, T.
1283   Alber, J. Thorner, and E. Nogales. 2008. Saccharomyces cerevisiae septins:
1284   supramolecular organization of heterooligomers and the mechanism of filament
1285   assembly. *Proc Natl Acad Sci U S A*. 105:8274-8279.
1286   Bertin, A., M.A. McMurray, J. Pierson, L. Thai, K.L. McDonald, E.A. Zehr, G. Garcia, 3rd,
1287   P. Peters, J. Thorner, and E. Nogales. 2012. Three-dimensional ultrastructure of
1288   the septin filament network in Saccharomyces cerevisiae. *Mol Biol Cell*. 23:423-
1289   432.
1290   Bertin, A., M.A. McMurray, L. Thai, G. Garcia, 3rd, V. Votin, P. Grob, T. Allyn, J. Thorner,
1291   and E. Nogales. 2010. Phosphatidylinositol-4,5-bisphosphate promotes budding

yeast septin filament assembly and organization. *Journal of molecular biology*. 404:711-731.

Bowen, J.R., D. Hwang, X. Bai, D. Roy, and E.T. Spiliotis. 2011. Septin GTPases spatially guide microtubule organization and plus end dynamics in polarizing epithelia. *The Journal of cell biology*. 194:187-197.

Bridges, A.A., M.S. Jentzsch, P.W. Oakes, P. Occhipinti, and A.S. Gladfelter. 2016. Micron-scale plasma membrane curvature is recognized by the septin cytoskeleton. *The Journal of cell biology*. 213:23-32.

Bridges, A.A., H. Zhang, S.B. Mehta, P. Occhipinti, T. Tani, and A.S. Gladfelter. 2014. Septin assemblies form by diffusion-driven annealing on membranes. *Proc Natl Acad Sci U S A*. 111:2146-2151.

Burrows, J.F., S. Chanduloy, M.A. McIlhatton, H. Nagar, K. Yeates, P. Donaghy, J. Price, A.K. Godwin, P.G. Johnston, and S.E. Russell. 2003. Altered expression of the septin gene, SEPT9, in ovarian neoplasia. *J Pathol*. 201:581-588.

Byers, B., and L. Goetsch. 1976. A highly ordered ring of membrane-associated filaments in budding yeast. *The Journal of cell biology*. 69:717-721.

Calvo, F., R. Ranftl, S. Hooper, A.J. Farrugia, E. Moeendarbary, A. Bruckbauer, F. Batista, G. Charras, and E. Sahai. 2015. Cdc42EP3/BORG2 and Septin Network Enables Mechano-transduction and the Emergence of Cancer-Associated Fibroblasts. *Cell Rep*. 13:2699-2714.

Camacho, C., G. Coulouris, V. Avagyan, N. Ma, J. Papadopoulos, K. Bealer, and T.L. Madden. 2009. BLAST+: architecture and applications. *BMC Bioinformatics*. 10:421.

Cao, L., X. Ding, W. Yu, X. Yang, S. Shen, and L. Yu. 2007. Phylogenetic and evolutionary analysis of the septin protein family in metazoan. *FEBS Lett*. 581:5526-5532.

Casamayor, A., and M. Snyder. 2003. Molecular dissection of a yeast septin: distinct domains are required for septin interaction, localization, and function. *Mol Cell Biol*. 23:2762-2777.

Castro, D., S.M.O. da Silva, H.D. Pereira, J.N.A. Macedo, D.A. Leonardo, N.F. Valadares, P.S. Kumagai, J. Brandao-Neto, A.P.U. Araujo, and R.C. Garratt. 2020. A complete compendium of crystal structures for the human SEPT3 subgroup reveals functional plasticity at a specific septin interface. *IUCrJ*. 7:462-479.

Collie, A.M., M.L. Landsverk, E. Ruzzo, H.C. Mefford, K. Buysse, J.R. Adkins, D.M. Knutzen, K. Barnett, R.H. Brown, Jr., G.J. Parry, S.W. Yum, D.A. Simpson, R.K. Olney, P.F. Chinnery, E.E. Eichler, P.F. Chance, and M.C. Hannibal. 2010. Non-recurrent SEPT9 duplications cause hereditary neuralgic amyotrophy. *J Med Genet*. 47:601-607.

Connolly, D., H.G. Hoang, E. Adler, C. Tazearslan, N. Simmons, V.V. Bernard, M. Castaldi, M.H. Oktay, and C. Montagna. 2014. Septin 9 amplification and isoform-specific expression in peritumoral and tumor breast tissue. *Biol Chem*. 395:157-167.

Connolly, D., Z. Yang, M. Castaldi, N. Simmons, M.H. Oktay, S. Coniglio, M.J. Fazzari, P. Verdier-Pinard, and C. Montagna. 2011. Septin 9 isoform expression, localization and epigenetic changes during human and mouse breast cancer progression. *Breast cancer research : BCR*. 13:R76.

Cordes, T., J. Vogelsang, and P. Tinnefeld. 2009. On the mechanism of Trolox as antiblinking and antibleaching reagent. *J Am Chem Soc*. 131:5018-5019.

Costantini, L.M., M. Fossati, M. Francolini, and E.L. Snapp. 2012. Assessing the tendency of fluorescent proteins to oligomerize under physiologic conditions. *Traffic*. 13:643-649.

Cranfill, P.J., B.R. Sell, M.A. Baird, J.R. Allen, Z. Lavagnino, H.M. de Gruiter, G.J. Kremers, M.W. Davidson, A. Ustione, and D.W. Piston. 2016. Quantitative assessment of fluorescent proteins. *Nature methods*. 13:557-562.

Damalio, J.C., T.M. Nobre, J.L. Lopes, O.N. Oliveira, Jr., and A.P. Araujo. 2013. Lipid interaction triggering Septin2 to assembly into beta-sheet structures investigated by Langmuir monolayers and PM-IRRAS. *Biochim Biophys Acta*. 1828:1441-1448.

de Almeida Marques, I., N.F. Valadares, W. Garcia, J.C. Damalio, J.N. Macedo, A.P. de Araujo, C.A. Botello, J.M. Andreu, and R.C. Garratt. 2012. Septin C-terminal domain interactions: implications for filament stability and assembly. *Cell Biochem Biophys*. 62:317-328.

Delorenzi, M., and T. Speed. 2002. An HMM model for coiled-coil domains and a comparison with PSSM-based predictions. *Bioinformatics*. 18:617-625.

DeRose, B.T., R.S. Kelley, R. Ravi, B. Kokona, J. Beld, E.T. Spiliotis, and S.B. Padrick. 2020. Production and analysis of a mammalian septin hetero-octamer complex. *Cytoskeleton (Hoboken)*. 77:485-499.

Diebold, M.L., S. Fribourg, M. Koch, T. Metzger, and C. Romier. 2011. Deciphering correct strategies for multiprotein complex assembly by co-expression: application to complexes as large as the histone octamer. *J Struct Biol*. 175:178-188.

Dolat, L., Q. Hu, and E.T. Spiliotis. 2014a. Septin functions in organ system physiology and pathology. *Biol Chem*. 395:123-141.

Dolat, L., J.L. Hunyara, J.R. Bowen, E.P. Karasmanis, M. Elgawly, V.E. Galkin, and E.T. Spiliotis. 2014b. Septins promote stress fiber-mediated maturation of focal adhesions and renal epithelial motility. *The Journal of cell biology*. 207:225-235.

Dolat, L., and E.T. Spiliotis. 2016. Septins promote macropinosome maturation and traffic to the lysosome by facilitating membrane fusion. *The Journal of cell biology*. 214:517-527.

Estey, M.P., C. Di Ciano-Oliveira, C.D. Froese, M.T. Bejide, and W.S. Trimble. 2010. Distinct roles of septins in cytokinesis: SEPT9 mediates midbody abscission. *The Journal of cell biology*. 191:741-749.

Farkasovsky, M., P. Herter, B. Voss, and A. Wittinghofer. 2005. Nucleotide binding and filament assembly of recombinant yeast septin complexes. *Biol Chem*. 386:643-656.

Field, C.M., O. al-Awar, J. Rosenblatt, M.L. Wong, B. Alberts, and T.J. Mitchison. 1996. A purified Drosophila septin complex forms filaments and exhibits GTPase activity. *The Journal of cell biology*. 133:605-616.

Fleming, P.J., and K.G. Fleming. 2018. HullRad: Fast Calculations of Folded and Disordered Protein and Nucleic Acid Hydrodynamic Properties. *Biophys J*. 114:856-869.

Frank, J., M. Radermacher, P. Penczek, J. Zhu, Y. Li, M. Ladjadj, and A. Leith. 1996. SPIDER and WEB: processing and visualization of images in 3D electron microscopy and related fields. *J Struct Biol*. 116:190-199.

Frazier, J.A., M.L. Wong, M.S. Longtine, J.R. Pringle, M. Mann, T.J. Mitchison, and C. Field. 1998. Polymerization of purified yeast septins: evidence that organized filament arrays may not be required for septin function. *The Journal of cell biology*. 143:737-749.

Fuchtbauer, A., L.B. Lassen, A.B. Jensen, J. Howard, S. Quiroga Ade, S. Warming, A.B. Sorensen, F.S. Pedersen, and E.M. Fuchtbauer. 2011. Septin9 is involved in septin filament formation and cellular stability. *Biol Chem*. 392:769-777.

Fung, K.Y., L. Dai, and W.S. Trimble. 2014. Cell and molecular biology of septins. *International review of cell and molecular biology*. 310:289-339.

Garcia, G., 3rd, A. Bertin, Z. Li, Y. Song, M.A. McMurray, J. Thorner, and E. Nogales. 2011. Subunit-dependent modulation of septin assembly: budding yeast septin Shs1 promotes ring and gauze formation. *The Journal of cell biology*. 195:993-1004.

Garcia, W., A.P. de Araujo, O. Neto Mde, M.R. Ballestero, I. Polikarpov, M. Tanaka, T. Tanaka, and R.C. Garratt. 2006. Dissection of a human septin: definition and characterization of distinct domains within human SEPT4. *Biochemistry*. 45:13918-13931.

Gruber, M., J. Soding, and A.N. Lupas. 2006. Comparative analysis of coiled-coil prediction methods. *J Struct Biol*. 155:140-145.

Guzenko, D., and S.V. Strelkov. 2018. CCFold: rapid and accurate prediction of coiled-coil structures and application to modelling intermediate filaments. *Bioinformatics*. 34:215-222.

Hall, P.A., E. Bruford, S.E.H. Russell, I.G. Macara, and J.R. Pringle. 2008. Mammalian septin nomenclature. *In* The Septins. P.A. Hall, S.E.H. Russell, and J.R. Pringle, editors. John Wiley & Sons, Ltd. 351-354.

Hall, P.A., K. Jung, K.J. Hillan, and S.E. Russell. 2005. Expression profiling the human septin gene family. *J Pathol*. 206:269-278.

Hannibal, M.C., E.K. Ruzzo, L.R. Miller, B. Betz, J.G. Buchan, D.M. Knutzen, K. Barnett, M.L. Landsverk, A. Brice, E. LeGuern, H.M. Bedford, B.B. Worrall, S. Lovitt, S.H. Appel, E. Andermann, T.D. Bird, and P.F. Chance. 2009. SEPT9 gene sequencing analysis reveals recurrent mutations in hereditary neuralgic amyotrophy. *Neurology*. 72:1755-1759.

Hartwell, L.H. 1971. Genetic control of the cell division cycle in yeast. IV. Genes controlling bud emergence and cytokinesis. *Experimental cell research*. 69:265-276.

Hartwell, L.H., J. Culotti, and B. Reid. 1970. Genetic control of the cell-division cycle in yeast. I. Detection of mutants. *Proc Natl Acad Sci U S A*. 66:352-359.

Hsu, S.C., C.D. Hazuka, R. Roth, D.L. Foletti, J. Heuser, and R.H. Scheller. 1998. Subunit composition, protein interactions, and structures of the mammalian brain sec6/8 complex and septin filaments. *Neuron*. 20:1111-1122.

Huijbregts, R.P., A. Svitin, M.W. Stinnett, M.B. Renfrow, and I. Chesnokov. 2009. Drosophila Orc6 facilitates GTPase activity and filament formation of the septin complex. *Mol Biol Cell*. 20:270-281.

John, C.M., R.K. Hite, C.S. Weirich, D.J. Fitzgerald, H. Jawhari, M. Faty, D. Schlapfer, R. Kroschewski, F.K. Winkler, T. Walz, Y. Barral, and M.O. Steinmetz. 2007. The Caenorhabditis elegans septin complex is nonpolar. *The EMBO journal*. 26:3296-3307.

Joo, E., M.C. Surka, and W.S. Trimble. 2007. Mammalian SEPT2 is required for scaffolding nonmuscle myosin II and its kinases. *Developmental cell*. 13:677-690.

Kelley, L.A., S. Mezulis, C.M. Yates, M.N. Wass, and M.J. Sternberg. 2015. The Phyre2 web portal for protein modeling, prediction and analysis. *Nat Protoc*. 10:845-858.

Kim, M.S., C.D. Froese, M.P. Estey, and W.S. Trimble. 2011. SEPT9 occupies the terminal positions in septin octamers and mediates polymerization-dependent functions in abscission. *The Journal of cell biology*. 195:815-826.

Kim, M.S., C.D. Froese, H. Xie, and W.S. Trimble. 2012. Uncovering principles that control septin-septin interactions. *The Journal of biological chemistry*. 287:30406-30413.

Kinoshita, M. 2003. Assembly of mammalian septins. *J Biochem*. 134:491-496.

Kinoshita, M., C.M. Field, M.L. Coughlin, A.F. Straight, and T.J. Mitchison. 2002. Self- and actin-templated assembly of Mammalian septins. *Developmental cell*. 3:791-802.

Kinoshita, M., S. Kumar, A. Mizoguchi, C. Ide, A. Kinoshita, T. Haraguchi, Y. Hiraoka, and M. Noda. 1997. Nedd5, a mammalian septin, is a novel cytoskeletal component interacting with actin-based structures. *Genes & development*. 11:1535-1547.

Kuhlenbaumer, G., M.C. Hannibal, E. Nelis, A. Schirmacher, N. Verpoorten, J. Meuleman, G.D. Watts, E. De Vriendt, P. Young, F. Stogbauer, H. Halfter, J. Irobi, D. Goossens, J. Del-Favero, B.G. Betz, H. Hor, G. Kurlemann, T.D. Bird, E. Airaksinen, T. Mononen, A.P. Serradell, J.M. Prats, C. Van Broeckhoven, P. De Jonghe, V. Timmerman, E.B. Ringelstein, and P.F. Chance. 2005. Mutations in SEPT9 cause hereditary neuralgic amyotrophy. *Nat Genet*. 37:1044-1046.

Kumagai, P.S., C.S. Martins, E.M. Sales, H.V.D. Rosa, D.C. Mendonca, J.C.P. Damalio, F. Spinozzi, R. Itri, and A.P.U. Araujo. 2019. Correct partner makes the difference: Septin G-interface plays a critical role in amyloid formation. *Int J Biol Macromol*. 133:428-435.

Landsverk, M.L., E.K. Ruzzo, H.C. Mefford, K. Buysse, J.G. Buchan, E.E. Eichler, E.M. Petty, E.A. Peterson, D.M. Knutzen, K. Barnett, M.R. Farlow, J. Caress, G.J. Parry, D. Quan, K.L. Gardner, M. Hong, Z. Simmons, T.D. Bird, P.F. Chance, and M.C. Hannibal. 2009. Duplication within the SEPT9 gene associated with a founder effect in North American families with hereditary neuralgic amyotrophy. *Hum Mol Genet*. 18:1200-1208.

Laue, T.M., B. Shah, T.M. Ridgeway, and S.L. Pelletier. 1992. Computer-aided interpretation of analytical sedimentation data for proteins. *In* Analytical Ultracentrifugation in Biochemistry and Polymer Science. S.E. Harding, J.C. Horton, and A.J. Rowe, editors. Royal Society of Chemistry. 90-125.

Liu, Z., Q.P. Vong, C. Liu, and Y. Zheng. 2014. Borg5 is required for angiogenesis by regulating persistent directional migration of the cardiac microvascular endothelial cells. *Mol Biol Cell*. 25:841-851.

Low, C., and I.G. Macara. 2006. Structural analysis of septin 2, 6, and 7 complexes. *The Journal of biological chemistry*. 281:30697-30706.

Ludtke, S.J., P.R. Baldwin, and W. Chiu. 1999. EMAN: semiautomated software for high-resolution single-particle reconstructions. *J Struct Biol*. 128:82-97.

Lupas, A., M. Van Dyke, and J. Stock. 1991. Predicting coiled coils from protein sequences. *Science*. 252:1162-1164.

Macara, I.G., R. Baldarelli, C.M. Field, M. Glotzer, Y. Hayashi, S.C. Hsu, M.B. Kennedy, M. Kinoshita, M. Longtine, C. Low, L.J. Maltais, L. McKenzie, T.J. Mitchison, T. Nishikawa, M. Noda, E.M. Petty, M. Peifer, J.R. Pringle, P.J. Robinson, D. Roth, S.E. Russell, H. Stuhlmann, M. Tanaka, T. Tanaka, W.S. Trimble, J. Ware, N.J. Zeleznik-Le, and B. Zieger. 2002. Mammalian septins nomenclature. *Mol Biol Cell*. 13:4111-4113.

Mackerell, A.D., Jr., M. Feig, and C.L. Brooks, 3rd. 2004. Extending the treatment of backbone energetics in protein force fields: limitations of gas-phase quantum mechanics in reproducing protein conformational distributions in molecular dynamics simulations. *J Comput Chem*. 25:1400-1415.

Marquardt, J., X. Chen, and E. Bi. 2019. Architecture, remodeling, and functions of the septin cytoskeleton. *Cytoskeleton (Hoboken)*. 76:7-14.

Mavrakis, M., Y. Azou-Gros, F.C. Tsai, J. Alvarado, A. Bertin, F. Iv, A. Kress, S. Brasselet, G.H. Koenderink, and T. Lecuit. 2014. Septins promote F-actin ring formation by crosslinking actin filaments into curved bundles. *Nature cell biology*. 16:322-334.

Mavrakis, M., F.C. Tsai, and G.H. Koenderink. 2016. Purification of recombinant human and Drosophila septin hexamers for TIRF assays of actin-septin filament assembly. *Methods Cell Biol*. 136:199-220.

McIlhatton, M.A., J.F. Burrows, P.G. Donaghy, S. Chanduloy, P.G. Johnston, and S.E. Russell. 2001. Genomic organization, complex splicing pattern and expression of a human septin gene on chromosome 17q25.3. *Oncogene*. 20:5930-5939.

McMurray, M.A., A. Bertin, G. Garcia, 3rd, L. Lam, E. Nogales, and J. Thorner. 2011. Septin filament formation is essential in budding yeast. *Developmental cell*. 20:540-549.

Mendonca, D.C., J.N. Macedo, S.L. Guimaraes, F.L. Barroso da Silva, A. Cassago, R.C. Garratt, R.V. Portugal, and A.P.U. Araujo. 2019. A revised order of subunits in mammalian septin complexes. *Cytoskeleton (Hoboken)*. 76:457-466.

Momany, M., F. Pan, and R.L. Malmberg. 2008. Evolution and conserved domains of the septins. *In* The Septins. P.A. Hall, S.E.H. Russell, and J.R. Pringle, editors. John Wiley & Sons, Ltd. 35-45.

Montagna, C., M. Bejerano-Sagie, and J.R. Zechmeister. 2015. Mammalian septins in health and disease. *Research and Reports in Biochemistry*. 5:59-72.

Mostowy, S., and P. Cossart. 2012. Septins: the fourth component of the cytoskeleton. *Nature reviews. Molecular cell biology*. 13:183-194.

Nagata, K., T. Asano, Y. Nozawa, and M. Inagaki. 2004. Biochemical and cell biological analyses of a mammalian septin complex, Sept7/9b/11. *The Journal of biological chemistry*. 279:55895-55904.

Nagata, K., A. Kawajiri, S. Matsui, M. Takagishi, T. Shiromizu, N. Saitoh, I. Izawa, T. Kiyono, T.J. Itoh, H. Hotani, and M. Inagaki. 2003. Filament formation of MSF-A, a mammalian septin, in human mammary epithelial cells depends on interactions with microtubules. *The Journal of biological chemistry*. 278:18538-18543.

Nakos, K., M. Rosenberg, and E.T. Spiliotis. 2019. Regulation of microtubule plus end dynamics by septin 9. *Cytoskeleton (Hoboken)*. 76:83-91.

Nishihama, R., M. Onishi, and J.R. Pringle. 2011. New insights into the phylogenetic distribution and evolutionary origins of the septins. *Biol Chem*. 392:681-687.

Omrane, M., A.S. Camara, C. Taveneau, N. Benzoubir, T. Tubiana, J. Yu, R. Guerois, D. Samuel, B. Goud, C. Pous, S. Bressanelli, R.C. Garratt, A.R. Thiam, and A. Gassama-Diagne. 2019. Septin 9 has Two Polybasic Domains Critical to Septin Filament Assembly and Golgi Integrity. *iScience*. 13:138-153.

Ong, K., C. Wloka, S. Okada, T. Svitkina, and E. Bi. 2014. Architecture and dynamic remodelling of the septin cytoskeleton during the cell cycle. *Nat Commun*. 5:5698.

Pan, F., R.L. Malmberg, and M. Momany. 2007. Analysis of septins across kingdoms reveals orthology and new motifs. *BMC evolutionary biology*. 7:103.
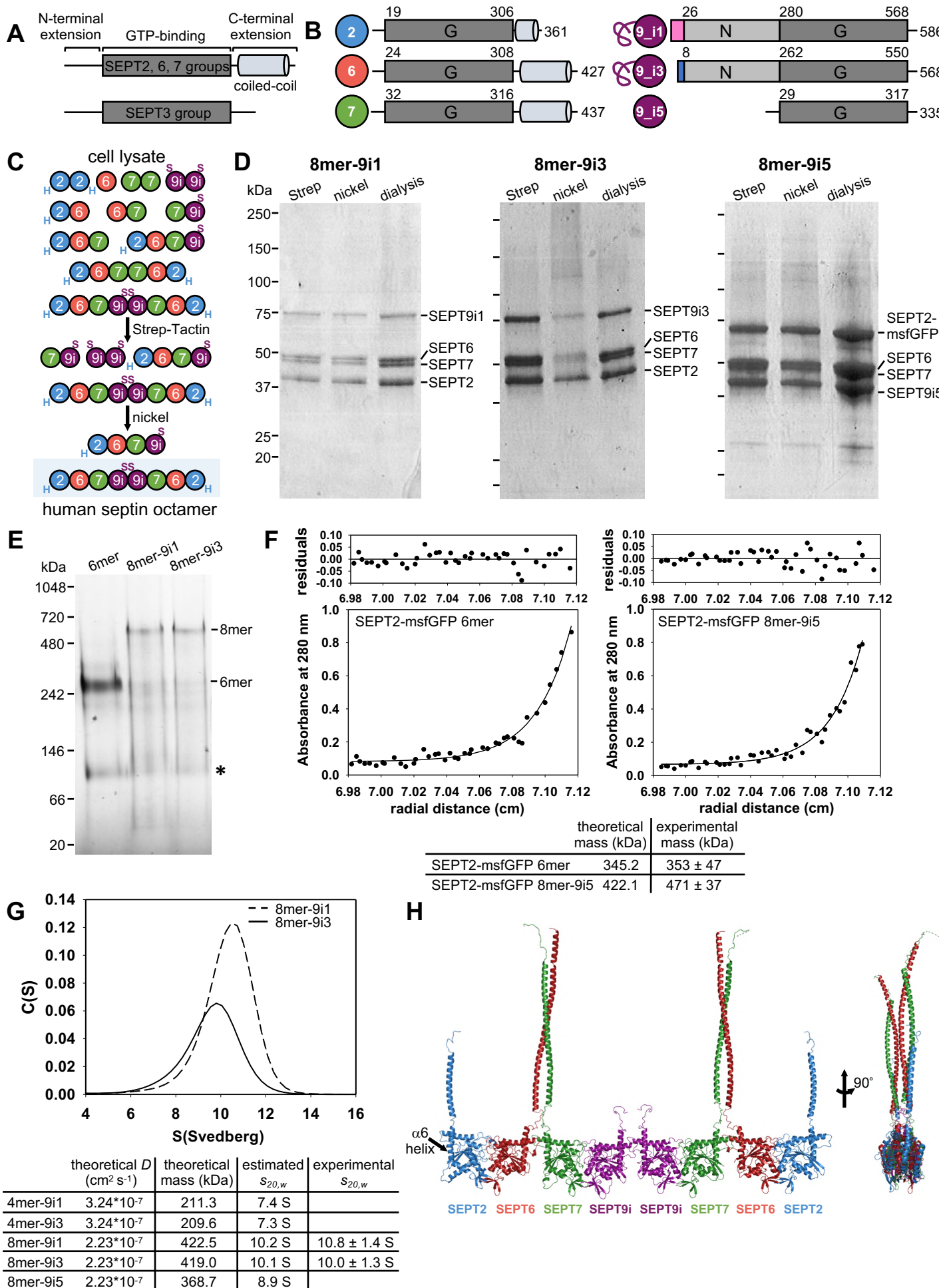
Pedelacq, J.D., S. Cabantous, T. Tran, T.C. Terwilliger, and G.S. Waldo. 2006. Engineering and characterization of a superfolder green fluorescent protein. *Nature biotechnology*. 24:79-88.

Pizarro-Cerda, J., R. Jonquieres, E. Gouin, J. Vandekerckhove, J. Garin, and P. Cossart. 2002. Distinct protein patterns associated with Listeria monocytogenes InlA- or InlB-phagosomes. *Cell Microbiol*. 4:101-115.

Rodal, A.A., L. Kozubowski, B.L. Goode, D.G. Drubin, and J.H. Hartwig. 2005. Actin and septin ultrastructures at the budding yeast cell cortex. *Mol Biol Cell*. 16:372-384.

Rosa, H.V.D., D.A. Leonardo, G. Brognara, J. Brandao-Neto, H. D'Muniz Pereira, A.P.U. Araujo, and R.C. Garratt. 2020. Molecular Recognition at Septin Interfaces: The Switches Hold the Key. *Journal of molecular biology*. 432:5784-5801.

Sala, F.A., N.F. Valadares, J.N. Macedo, J.C. Borges, and R.C. Garratt. 2016. Heterotypic Coiled-Coil Formation is Essential for the Correct Assembly of the Septin Heterofilament. *Biophys J*. 111:2608-2619.

Schuck, P., and P. Rossmanith. 2000. Determination of the sedimentation coefficient distribution by least-squares boundary modeling. *Biopolymers*. 54:328-341.

Sellin, M.E., L. Sandblad, S. Stenmark, and M. Gullberg. 2011. Deciphering the rules governing assembly order of mammalian septin complexes. *Mol Biol Cell*. 22:3152-3164.

Sellin, M.E., S. Stenmark, and M. Gullberg. 2014. Cell type-specific expression of SEPT3-homology subgroup members controls the subunit number of heteromeric septin complexes. *Mol Biol Cell*. 25:1594-1607.

Shevchenko, A., H. Tomas, J. Havlis, J.V. Olsen, and M. Mann. 2006. In-gel digestion for mass spectrometric characterization of proteins and proteomes. *Nat Protoc*. 1:2856-2860.

Shi, X., J. Lim, and T. Ha. 2010. Acidification of the oxygen scavenging system in single-molecule fluorescence studies: in situ sensing with a ratiometric dual-emission probe. *Anal Chem*. 82:6132-6138.

Silva, J.C., M.V. Gorenstein, G.Z. Li, J.P. Vissers, and S.J. Geromanos. 2006. Absolute quantification of proteins by LCMSE: a virtue of parallel MS acquisition. *Mol Cell Proteomics*. 5:144-156.

Sirajuddin, M., M. Farkasovsky, F. Hauer, D. Kuhlmann, I.G. Macara, M. Weyand, H. Stark, and A. Wittinghofer. 2007. Structural insight into filament formation by mammalian septins. *Nature*. 449:311-315.

Smith, C., L. Dolat, D. Angelis, E. Forgacs, E.T. Spiliotis, and V.E. Galkin. 2015. Septin 9 Exhibits Polymorphic Binding to F-Actin and Inhibits Myosin and Cofilin Activity. *Journal of molecular biology*. 427:3273-3284.

Soroor, F., M.S. Kim, O. Palander, Y. Balachandran, R.F. Collins, S. Benlekbir, J. Rubinstein, and W.S. Trimble. 2020. Revised subunit order of mammalian septin complexes explains their in-vitro polymerization properties. *Mol Biol Cell*:mbcE20060398.

Spiliotis, E.T., S.J. Hunt, Q. Hu, M. Kinoshita, and W.J. Nelson. 2008. Epithelial polarity requires septin coupling of vesicle transport to polyglutamylated microtubules. *The Journal of cell biology*. 180:295-303.

Spiliotis, E.T., M. Kinoshita, and W.J. Nelson. 2005. A mitotic septin scaffold required for Mammalian chromosome congression and segregation. *Science*. 307:1781-1785.
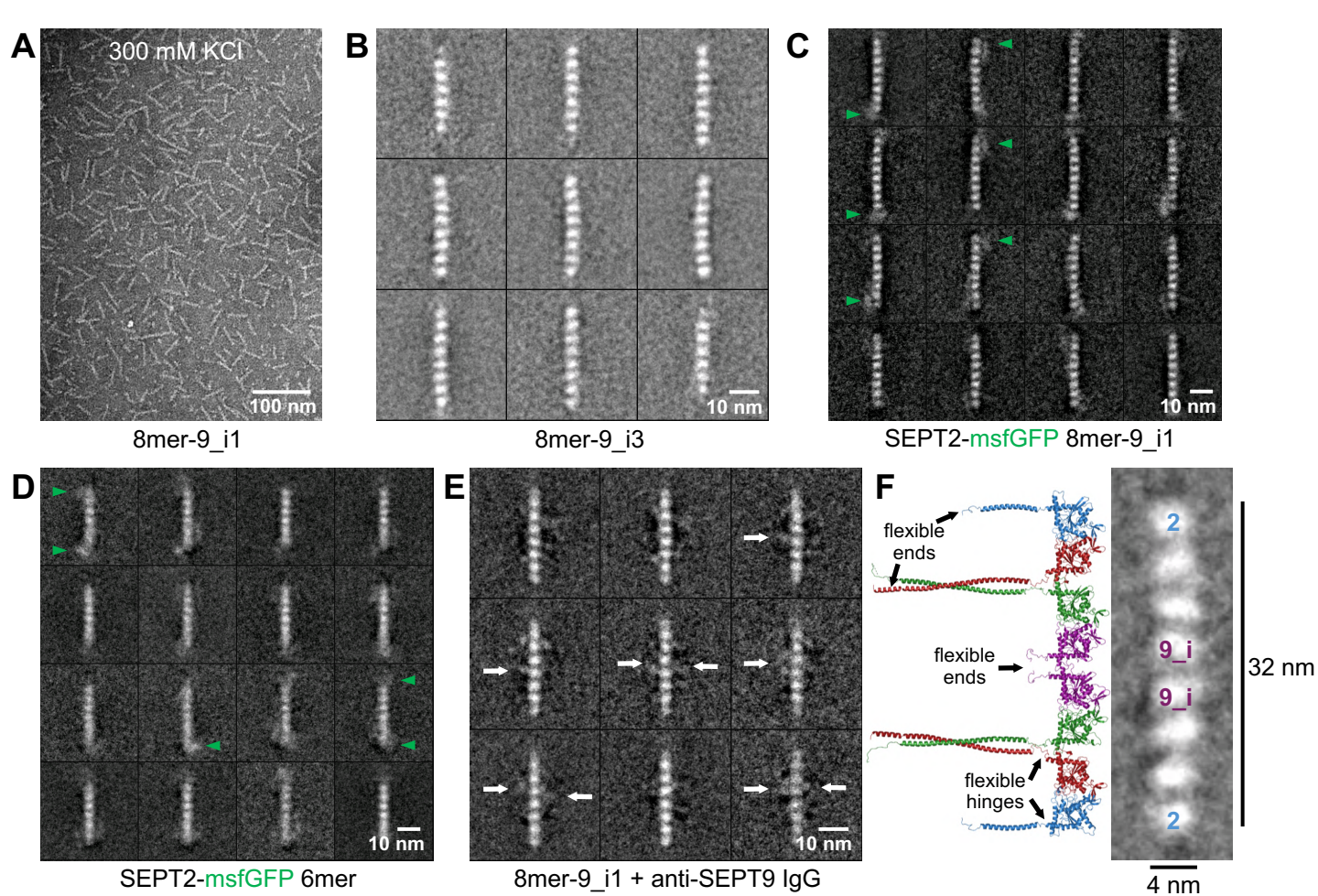
Steinegger, M., M. Meier, M. Mirdita, H. Vohringer, S.J. Haunsberger, and J. Soding. 2019. HH-suite3 for fast remote homology detection and deep protein annotation. *BMC Bioinformatics*. 20:473.

Studer, G., C. Rempfer, A.M. Waterhouse, R. Gumienny, J. Haas, and T. Schwede. 2020. QMEANDisCo-distance constraints applied on model quality estimation. *Bioinformatics*. 36:2647.

Surka, M.C., C.W. Tsang, and W.S. Trimble. 2002. The mammalian septin MSF localizes with microtubules and is required for completion of cytokinesis. *Mol Biol Cell*. 13:3532-3545.

Tanaka-Takiguchi, Y., M. Kinoshita, and K. Takiguchi. 2009. Septin-mediated uniform bracing of phospholipid membranes. *Curr Biol*. 19:140-145.

Taveneau, C., R. Blanc, G. Pehau-Arnaudet, A. Di Cicco, and A. Bertin. 2020. Synergistic role of nucleotides and lipids for the self-assembly of Shs1 septin oligomers. *Biochem J*. 477:2697-2714.

Taylor, I.A., K. Rittinger, and J.F. Eccleston. 2015. Sedimentation Equilibrium Studies. *In* Methods in Molecular Biology. Vol. 1278. C.L. Meyerkord and H. Fu, editors. Springer. 205-222.

Valadares, N.F., H. d' Muniz Pereira, A.P. Ulian Araujo, and R.C. Garratt. 2017. Septin structure and filament assembly. *Biophys Rev*. 9:481-500.

Verdier-Pinard, P., D. Salaun, H. Bouguenina, S. Shimada, M. Pophillat, S. Audebert, E. Agavnian, S. Coslet, E. Charafe-Jauffret, T. Tachibana, and A. Badache. 2017. Septin 9_i2 is downregulated in tumors, impairs cancer cell migration and alters subnuclear actin filaments. *Sci Rep*. 7:44976.

Versele, M., and J. Thorner. 2004. Septin collar formation in budding yeast requires GTP binding and direct phosphorylation by the PAK, Cla4. *The Journal of cell biology*. 164:701-715.

Waterhouse, A., M. Bertoni, S. Bienert, G. Studer, G. Tauriello, R. Gumienny, F.T. Heer, T.A.P. de Beer, C. Rempfer, L. Bordoli, R. Lepore, and T. Schwede. 2018. SWISS-MODEL: homology modelling of protein structures and complexes. *Nucleic Acids Res*. 46:W296-W303.

Weems, A., and M. McMurray. 2017. The step-wise pathway of septin hetero-octamer assembly in budding yeast. *Elife*. 6.

Weirich, C.S., J.P. Erzberger, and Y. Barral. 2008. The septin family of GTPases: architecture and dynamics. *Nature reviews. Molecular cell biology*. 9:478-489.

Winkelman, J.D., C. Suarez, G.M. Hocky, A.J. Harker, A.N. Morganthaler, J.R. Christensen, G.A. Voth, J.R. Bartles, and D.R. Kovar. 2016. Fascin- and alpha-Actinin-Bundled Networks Contain Intrinsic Structural Features that Drive Protein Sorting. *Curr Biol*. 26:2697-2706.

Xie, H., M. Surka, J. Howard, and W.S. Trimble. 1999. Characterization of the mammalian septin H5: distinct patterns of cytoskeletal and membrane association from other septin proteins. *Cell motility and the cytoskeleton*. 43:52-62.

Zacharias, D.A., J.D. Violin, A.C. Newton, and R.Y. Tsien. 2002. Partitioning of lipid-modified monomeric GFPs into membrane microdomains of live cells. *Science*. 296:913-916.

Zhang, J., C. Kong, H. Xie, P.S. McPherson, S. Grinstein, and W.S. Trimble. 1999. Phosphatidylinositol polyphosphate binding to the mammalian septin H5 is modulated by GTP. *Curr Biol*. 9:1458-1467.

1622   Zimmermann, L., A. Stephens, S.Z. Nam, D. Rau, J. Kubler, M. Lozajic, F. Gabler, J.
1623   Soding, A.N. Lupas, and V. Alva. 2018. A Completely Reimplemented MPI
1624   Bioinformatics Toolkit with a New HHpred Server at its Core. *Journal of molecular*
1625   *biology*. 430:2237-2243.
1626
1627

Figure 1
Iv et al 2020

A 300 mM KCl
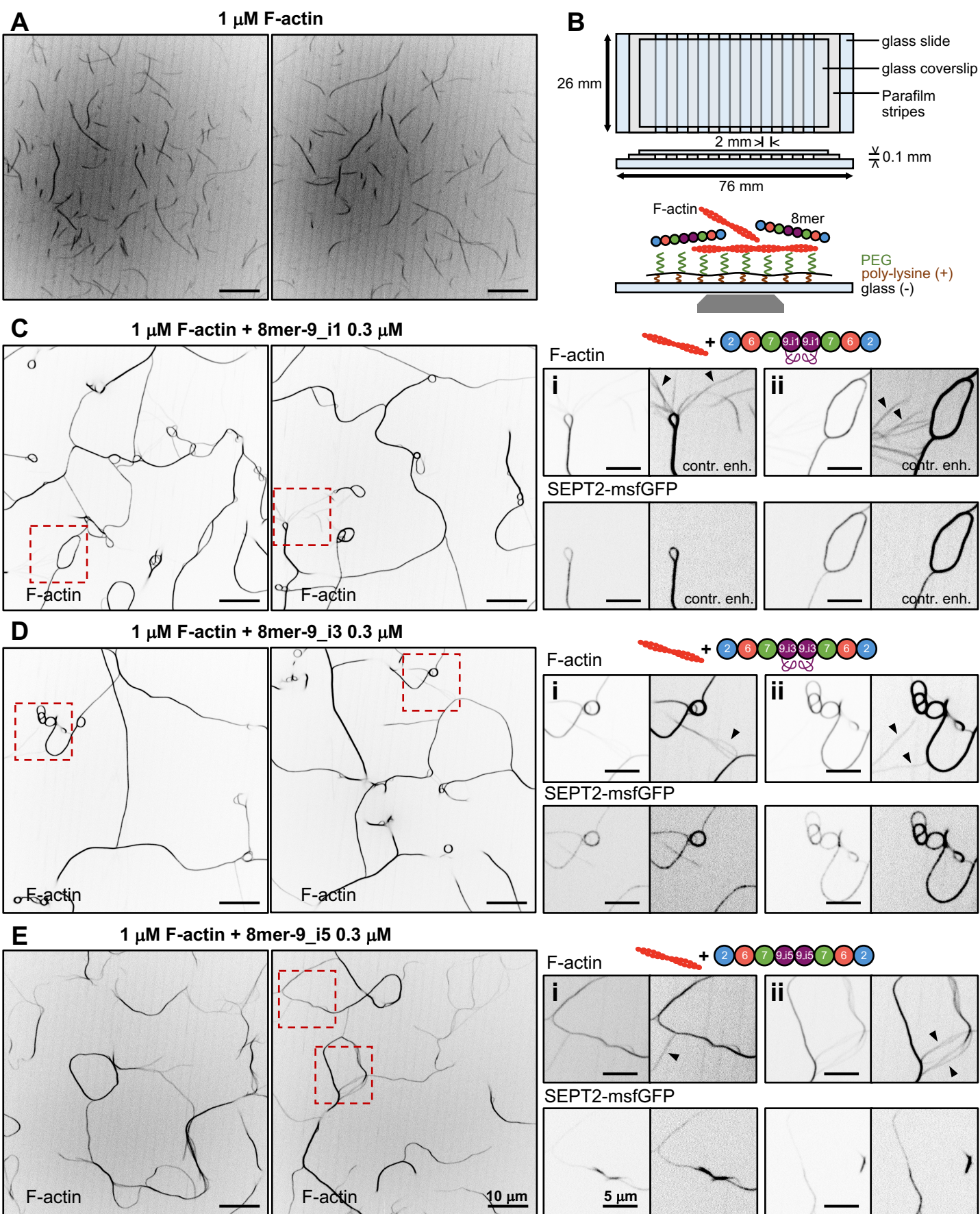8mer-9_i1

B 8mer-9_i3

C SEPT2-msfGFP 8mer-9_i1

D SEPT2-msfGFP 6mer

E 8mer-9_i1 + anti-SEPT9 IgG

F
flexible ends
flexible ends
flexible hinges

2
9_i
9_i
2

32 nm

Figure 2
Iv et al 2020

Figure 3
Iv et al 2020

A 1 μM F-actin

B
glass slide
glass coverslip
Parafilm stripes
26 mm
2 mm
0.1 mm
76 mm

F-actin   8mer
PEG
poly-lysine (+)
glass (−)

C 1 μM F-actin + 8mer-9_i1 0.3 μM

F-actin

2 6 7 9_i1 9_i1 7 6 2

F-actin

i   contr. enh.
ii   contr. enh.

SEPT2-msfGFP

contr. enh.   contr. enh.

D 1 μM F-actin + 8mer-9_i3 0.3 μM

F-actin

2 6 7 9_i3 9_i3 7 6 2

F-actin

i   **ii**

SEPT2-msfGFP

E 1 μM F-actin + 8mer-9_i5 0.3 μM

F-actin

2 6 7 9_i5 9_i5 7 6 2

F-actin

10 μm

i   **ii**

SEPT2-msfGFP

5 μm

Figure 4
Iv et al 2020